The Astrophysical Journal, 678:985–1004, 2008 May 10

THE c2d *SPITZER* SPECTROSCOPIC SURVEY OF ICES AROUND LOW-MASS YOUNG STELLAR OBJECTS. I. H_2O AND THE 5–8 μm BANDS[1,2]

A. C. A. Boogert,[3,4,5] K. M. Pontoppidan,[6,7] C. Knez,[8] F. Lahuis,[9,10] J. Kessler-Silacci,[11] E. F. van Dishoeck,[9] G. A. Blake,[6] J.-C. Augereau,[12] S. E. Bisschop,[9] S. Bottinelli,[9] T. Y. Brooke,[13] J. Brown,[3] A. Crapsi,[9] N. J. Evans II,[11] H. J. Fraser,[14] V. Geers,[9] T. L. Huard,[15] J. K. Jørgensen,[15] K. I. Öberg,[9] L. E. Allen,[15] P. M. Harvey,[11] D. W. Koerner,[16] L. G. Mundy,[8] D. L. Padgett,[13] A. I. Sargent,[3] and K. R. Stapelfeldt[17]

Received 2007 September 23; accepted 2008 January 5

ABSTRACT

To study the physical and chemical evolution of ices in solar-mass systems, a spectral survey is conducted of a sample of 41 low-luminosity YSOs ($L \sim 0.1$–$10\ L_\odot$) using 3–38 μm *Spitzer* and ground-based spectra. The sample is complemented with previously published *Spitzer* spectra of background stars and with *ISO* spectra of well-studied massive YSOs ($L \sim 10^5\ L_\odot$). The long-known 6.0 and 6.85 μm bands are detected toward all sources, with the Class 0–type YSOs showing the deepest bands ever observed. The 6.0 μm band is often deeper than expected from the bending mode of pure solid H_2O. The additional 5–7 μm absorption consists of five independent components, which, by comparison to laboratory studies, must be from at least eight different carriers. Much of this absorption is due to simple species likely formed by grain surface chemistry, at abundances of 1%–30% for CH_3OH, 3%–8% for NH_3, 1%–5% for HCOOH, ~6% for H_2CO, and ~0.3% for $HCOO^-$ relative to solid H_2O. The 6.85 μm band has one or two carriers, of which one may be less volatile than H_2O. Its carrier(s) formed early in the molecular cloud evolution and do not survive in the diffuse ISM. If an NH_4^+-containing salt is the carrier, its abundance relative to solid H_2O is ~7%, demonstrating the efficiency of low-temperature acid-base chemistry or cosmic-ray–induced reactions. Possible origins are discussed for enigmatic, very broad absorption between 5 and 8 μm. Finally, the same ices are observed toward massive and low-mass YSOs, indicating that processing by internal UV radiation fields is a minor factor in their early chemical evolution.

Subject headings: astrochemistry — infrared: ISM — infrared: stars — ISM: abundances — ISM: molecules — stars: formation

Online material: machine-readable table

1. INTRODUCTION

The infrared spectra of protostars and obscured background stars show prominent absorption features at 3.0, 4.25, 4.7, 6.0, 6.85, 9.7, and 15 μm along with a suite of weaker features (e.g., d'Hendecourt et al. 1996; Whittet et al. 1996, 2007; Gerakines et al. 1999; Schutte et al. 1999; Gibb et al. 2000, 2004; Keane et al. 2001b; Pontoppidan et al. 2003b; Knez et al. 2005; for a complete list of features see Boogert & Ehrenfreund 2004). These are attributed to absorption in the vibrational modes of molecules in ices, except for the 9.7 μm band, which is mostly due to silicates. At the low temperatures ($T \leq 20$ K) of dense clouds and circumprotostellar environments atoms and molecules freeze out rapidly on dust grains. Grain surface chemistry efficiently forms new, simple species, such as H_2O and H_2CO (e.g., Tielens & Hagen 1982). Complex species (e.g., polyoxymethylene ["POM," $(-CH_2-O-)_n$] and hexamethylenetetramine ["HMT," $C_6H_{12}N_4$]) can be formed through the impact of energetic photons or cosmic rays on the ices, as many laboratory studies have shown (e.g., Schutte et al. 1993; Bernstein et al. 1995; Greenberg et al. 1995; Gerakines et al. 1996; Moore & Hudson 1998; Palumbo et al. 2000; Muñoz Caro et al. 2004). Thus far, only the simple species H_2O, CO, CO_2, CH_4, CH_3OH, and NH_3 and the ^{13}CO and $^{13}CO_2$ isotopes have been positively identified in the ices toward both low- and high-mass protostars, as well as extincted background stars whose lines of sight trace quiescent dense cloud material. Reasonable evidence exists for the presence of HCOOH, H_2CO, OCS, and the ions NH_4^+, OCN^-, and $HCOO^-$ as well, although their existence is sometimes debated because of inaccurate fits with laboratory

[1] Some of the data presented herein were obtained at the W. M. Keck Observatory, which is operated as a scientific partnership among the California Institute of Technology, the University of California, and the National Aeronautics and Space Administration. The Observatory was made possible by the generous financial support of the W. M. Keck Foundation.

[2] The VLT ISAAC spectra were obtained at the European Southern Observatory, Paranal, Chile, within the observing programs 164.I-0605, 69.C-0441, and 272.C-5008.

[3] Division of PMA, California Institute of Technology, Pasadena, CA 91125.

[4] AURA/NOAO-South, Gemini Science Center, Casilla 603, La Serena, Chile.

[5] Current address: IPAC, NASA Herschel Science Center, Mail Code 100-22, California Institute of Technology, Pasadena, CA 91125; aboogert@ipac.caltech.edu.

[6] Division of GPS, California Institute of Technology, Pasadena, CA 91125.

[7] Hubble Fellow.

[8] Department of Astronomy, University of Maryland, College Park, MD 20742.

[9] Leiden Observatory, Leiden University, 2300 RA Leiden, Netherlands.

[10] SRON, 9700 AV Groningen, Netherlands.

[11] Department of Astronomy, University of Texas at Austin, Austin, TX 78712-0259.

[12] Laboratoire d'Astrophysique de Grenoble, CNRS, Université Joseph-Fourier, UMR 5571, Grenoble, France.

[13] *Spitzer* Science Center, California Institute of Technology, Pasadena, CA 91125.

[14] Department of Physics, Scottish Universities Physics Alliance (SUPA), University of Strathclyde, Glasgow G4 ONG, UK.

[15] Smithsonian Astrophysical Observatory, Cambridge, MA 02138.

[16] Department of Physics and Astronomy, Northern Arizona University, Flagstaff, AZ 86011-6010.

[17] Jet Propulsion Laboratory, California Institute of Technology, Pasadena, CA 91109.

spectra or the lack of multiple bands for independent confirmation. The identification of the ions in the ices has been particularly controversial. The first ion claimed was OCN^- (Grim & Greenberg 1987) and was thought to be produced by heavy energetic processing of $CO:NH_3$ ices. Later it was realized that acid-base chemistry in an $HNCO:NH_3$ ice could yield the same products (Novozamsky et al. 2001). Acid-base reactions are very efficient and occur at temperatures as low as 10 K (Raunier et al. 2004b). The created ions are less volatile than neutral species and would be able to form an interstellar salt after the other species have sublimated. The presence of complex species formed by ultraviolet (UV) photon and cosmic-ray processing of the simple ices is at least as controversial. Many claims were made (Greenberg et al. 1995; Gibb & Whittet 2002), but the observational evidence is not firm. It is crucial to determine the complexity of the ices in the circumstellar environment of low-mass young stellar objects (YSOs), as they may be delivered directly to comets and they may ultimately serve as the source of volatiles in planets. At sublimation fronts in the warm inner regions of disks they are the starting point of a complex gas-phase chemistry. The relative abundances of N-, C-, and O-bearing species coming from the ices determine directly the type of chemistry in hot cores (or "hot corinos" for low-mass objects; e.g., Cazaux et al. 2003).

As a step toward better characterizing the molecular content of icy grain mantles, this work presents spectra of a large sample of low-mass protostars and background stars obtained with the Infrared Spectrometer (IRS; Houck et al. 2004) at the *Spitzer Space Telescope* (Werner et al. 2004) in the 5–35 μm wavelength range. These data are complemented with spectra at 2–4 μm obtained with ground-based facilities. Such full coverage over the near- and mid-infrared wavelength ranges is essential in determining the composition of the ices; most species have several vibrational modes, and more secure identifications can be made when the features are studied simultaneously. The identification process is aided by studying large samples of sight lines facilitating correlation of band strengths and shapes with each other and, if known, with physical characteristics along the sight lines, such as luminosity and evolutionary stage of any heating source. The great sensitivity of the IRS allows for observations of objects with luminosities that are down by orders of magnitude with respect to what could be observed before in the mid-infrared (typically 1 $L_\odot$ vs. 10^4 $L_\odot$).

Most data presented in this paper were obtained from spectral surveys of nearby molecular clouds and isolated dense cores in the context of the *Spitzer* Legacy Program "From Molecular Cores to Planet-Forming Disks" ("c2d"; Evans et al. 2003). Initial results from this program emphasize the importance of thermal processing in the evolution of the ices, as the ices surrounding the low-mass YSO HH 46 IRS are more processed compared to B5 IRS 1 (Boogert et al. 2004). Ices toward the edge-on disk CRBR 2422.8−3423 were presented in Pontoppidan et al. (2005) and also show signs of heating. Finally, mid-infrared spectra of ices toward background stars tracing quiescent cloud material were published in Knez et al. (2005), showing for the first time that the (unknown) carrier of the 6.85 μm absorption band is abundant even at the coldest conditions away from star formation.

This paper specifically addresses questions on the identification of the 6.0 and 6.85 μm bands. These prominent absorption features are still not fully identified, despite being detected nearly 30 years ago with the Kuiper Airborne Observatory (Puetter et al. 1979) and commonly observed toward massive YSOs with the *Infrared Space Observatory* (*ISO*; Schutte et al. 1996; Keane et al. 2001b). The peak position of the 6.85 μm band varies dramatically and is thought to be a function of the ice temperature (Keane et al. 2001b). Either one carrier with a pronounced temperature dependence of its absorption bands or two independent carriers, one much more volatile than the other, must be responsible for the 6.85 μm feature. If the former is the case, the ammonium ion (NH_4^+) is considered a promising candidate (Schutte & Khanna 2003). The 6.0 μm band was initially thought to be mainly due to the bending mode of H_2O (Tielens et al. 1984; however, see Cox 1989), but analysis of *ISO* spectra indicated that this is not the case toward several massive YSOs (Schutte et al. 1996; Keane et al. 2001b). The depth of the 6.0 μm band is in some cases significantly (factor of 2) deeper than that expected from the 3.0 μm H_2O stretching mode. Part of this "excess" might be due to a strong vibration of the HCOOH molecule. Recent observations of background stars show a small excess ($\leq$25%), of which half could be due to the enhanced band strength of the H_2O bending mode in CO_2-rich ices (Knez et al. 2005). Finally, it was claimed that much of the 6.0 μm excess and part of the 6.85 μm band is due to highly processed ices, i.e., a mixture of complex species with C−H and O−H bonds produced after irradiation of simple ices (Gibb & Whittet 2002). In this case, one would expect the 6.0 μm excess to be enhanced in high-radiation environments, such as near more evolved protostars. Thus, fundamental questions remain on the identification of the 6.0 and 6.85 μm bands, and with the large sample presented in this work the possible answers can be further constrained. Subsequent papers will specifically address the CO_2 (Pontoppidan et al. 2008), CH_4 (Öberg et al. 2008), and NH_3 (S. Bottinelli et al. 2008, in preparation) species. Further papers in this series will investigate the ices toward background stars behind large clouds (C. Knez et al. 2008, in preparation) and isolated cores (A. C. A. Boogert et al. 2008, in preparation).

In § 2 the source sample is presented, while the observations and data reduction of the ground-based *L*-band and *Spitzer* 5–38 μm spectra are described in § 3. In § 4 the continuum level for the multitude of absorption features is determined, and subsequently the best value for the H_2O column density derived, followed by an empirical decomposition of the 5–7 μm absorption complex. The positively identified species, or correlations of the components with other observables, are discussed in § 5. Finally, the abundances of the simple species and constraints on the carriers of unidentified components are discussed in § 6.

2. SOURCE SAMPLE

The source sample is selected based on the presence of ice absorption features and consists of a combination of known low-mass YSOs and new ones identified from their *Spitzer* IRAC and MIPS broadband spectral energy distributions (SEDs; Table 1; Evans et al. 2007[18]). For the known objects, their mid-infrared (5–20 μm) spectra are presented here for the first time, with the exception of B5 IRS 1, HH 46 IRS (Boogert et al. 2004; Noriega-Crespo et al. 2004), CRBR 2422.8−3423 (Pontoppidan et al. 2005), L1489 IRS, IRAS 04108+2803B, HH 300, and DG Tau B (Watson et al. 2004). The YSOs are located in the Perseus, Taurus, Serpens, and Corona Australis molecular cloud complexes and a number of nearby isolated dense cores (Table 1). YSOs in the Ophiuchus cloud are notably absent because the *Spitzer* IRS spectra were not available at the time this paper was written. The SEDs of the sample of 41 low-mass YSOs span a wide range of spectral indices $\alpha = -0.25$ to +2.70, with α defined as

$$\alpha = \frac{d \log(\lambda F_\lambda)}{d \log \lambda}, \quad (1)$$

[18] Available at http://ssc.spitzer.caltech.edu/legacy/.

TABLE 1

SOURCE SAMPLE

Source	Alias	R.A.[a] (J2000.0)	Decl.[a] (J2000.0)	Cloud	Type[b]	α_{IR}[c]	ObsID[d]	Module[e]	L Band[f]
L1448 IRS 1	RNO 13	03 25 09.44	+30 46 21.7	Perseus	Low	0.34	0005656832	SL, SH, LH	NIRSPEC
IRAS 03235+3004		03 26 37.45	+30 15 27.9	Perseus	Low	1.44	0009835520	SL, LL	NIRSPEC
IRAS 03245+3002		03 27 39.03	+30 12 59.3	Perseus	Low	2.70	0006368000	SL, SH	
L1455 SMM 1		03 27 43.25	+30 12 28.8	Perseus	Low	2.41	0015917056	SL, SH, LL1	
RNO 15	IRAS 03247+3001	03 27 47.68	+30 12 04.3	Perseus	Low	−0.21	0005633280	LL1, SL, SH, LH	NIRSPEC
L1455 IRS 3		03 28 00.41	+30 08 01.2	Perseus	Low	0.98	0015917568	SL, SH, LL1	
IRAS 03254+3050		03 28 34.51	+31 00 51.2	Perseus	Low	0.90	0011827200	LL1, SL, SH, LH	NIRSPEC
IRAS 03271+3013		03 30 15.16	+30 23 48.8	Perseus	Low	2.06	0005634304	LL1, SL, SH, LH	NIRSPEC
IRAS 03301+3111		03 33 12.85	+31 21 24.2	Perseus	Low	0.51	0005634560	SL, SH, LH	NIRSPEC
B1-a		03 33 16.67	+31 07 55.1	Perseus	Low	1.87	0015918080	SL, SH, LL1	NIRSPEC
B1-c		03 33 17.89	+31 09 31.0	Perseus	Low	2.66	0013460480	SL, SH, LL1	
B1-b		03 33 20.34	+31 07 21.4	Perseus	Low	0.68	0015916544	SL, LL	
B5 IRS 3	IRAS 03439+3233	03 47 05.45	+32 43 08.5	Perseus	Low	0.51[g]	0005635072	LL1, SL, SH, LH	NIRSPEC
B5 IRS 1[h]	IRAS 03445+3242	03 47 41.61	+32 51 43.8	Perseus	Low	0.78[g]	0005635328	SL, SH, LH	NIRSPEC
L1489 IRS[i]	IRAS 04016+2610	04 04 43.07	+26 18 56.4	Taurus	Low	1.10	0003528960	SL, SH, LH	NIRSPEC
IRAS 04108+2803B[i]		04 13 54.72	+28 11 32.9	Taurus	Low	0.90	0003529472	SL, SH, LH	NIRSPEC
HH 300[i]	IRAS 04239+2436	04 26 56.30	+24 43 35.3	Taurus	Low	0.79	0003530752	SL, SH, LH	NIRSPEC
DG Tau B[i]		04 27 02.66	+26 05 30.5	Taurus	Low	1.16	0003540992	SL, SH, LH	NIRSPEC
HH 46 IRS[h]	IRAS 08242−5050	08 25 43.78	−51 00 35.6	HH 46	Low	1.70	0005638912	SL, SH, LH	ISAAC
IRAS 12553−7651		12 59 06.63	−77 07 40.0	Cha	Low	0.76	0009830912	LL1, SL, SH, LH	
IRAS 13546−3941		13 57 38.94	−39 56 00.2	BHR 92	Low	−0.06	0005642752	SL, SH, LH	
IRAS 15398−3359		15 43 02.26	−34 09 06.7	B228	Low	1.22	0005828864	SL, SH, LL1	
Elias 29[j]		16 27 09.42	−24 37 21.1	Oph	Low	0.53[g]	26700814	SWS01 sp3	
CRBR 2422.8−3423[k]		16 27 24.61	−24 41 03.3	Oph	Low	1.36	0009346048	SL, SH, LH	NIRSPEC
RNO 91	IRAS 16316−1540	16 34 29.32	−15 47 01.4	L43	Low	0.03	0005650432	SL, SH, LH	ISAAC
IRAS 17081−2721	[BHB2007] 7	17 11 17.28	−27 25 08.2	B59	Low	0.55	0014893824	SL, SH, LL1	NIRSPEC
SSTc2d J171122.2−272602	[BHB2007] 10	17 11 22.16	−27 26 02.3	B59	Low	2.26	0014894336	SL, LL	
2MASS J17112317−2724315	[BHB2007] 11	17 11 23.13	−27 24 32.6	B59	Low	2.48	0014894592	SL, LL	NIRSPEC
EC 74	CK 9	18 29 55.72	+01 14 31.6	Serpens	Low	−0.25	0009407232	SL, SH, LH	NIRSPEC
EC 82	CK 3, SVS 2	18 29 56.89	+01 14 46.5	Serpens	Low	0.38[g]	0009407232	SL, SH, LH	
SVS 4-5		18 29 57.59	+01 13 00.6	Serpens	Low	1.26	0009407232	SL, SH, LH	ISAAC
EC 90	CK 1, SVS 20	18 29 57.75	+01 14 05.9	Serpens	Low	−0.09	0009828352	SL, SH, LH	
EC 92	SVS 4-10	18 29 57.88	+01 12 51.6	Serpens	Low	0.91	0009407232	SL, SH, LH	NIRSPEC
CK 4	EC 97	18 29 58.21	+01 15 21.7	Serpens	Low	−0.25	0009407232	SL, SH, LH	
R CrA IRS 5		19 01 48.03	−36 57 21.6	CrA	Low	0.98	0009835264	SL, SH, LL1	ISAAC
HH 100 IRS[l]		19 01 50.56	−36 58 08.9	CrA	Low	0.80	52301106	SWS01 sp4	
CrA IRS 7A		19 01 55.32	−36 57 22.0	CrA	Low	2.23	0009835008	SL, SH, LH	ISAAC
CrA IRS 7B		19 01 56.41	−36 57 28.0	CrA	Low	1.63	0009835008	SL, SH, LH	ISAAC
CrA IRAS 32		19 02 58.69	−37 07 34.5	CrA	Low	2.15	0009832192	SL, SH, LL1	
L1014 IRS		21 24 07.51	+49 59 09.0	L1014	Low	1.28	0012116736	SL, LL	NIRSPEC
IRAS 23238+7401		23 25 46.65	+74 17 37.2	CB 244	Low	0.95	0009833728	SL, SH, LH	NIRSPEC
W3 IRS 5[l]		02 25 40.54	+62 05 51.4		High	3.53	42701302	SWS01 sp3	
Mon R2 IRS 3[l]		06 07 47.8	−06 22 55.0		High	1.66	71101712	SWS01 sp3	
GL 989[l]		06 41 10.06	+09 29 35.8		High	0.52	71602619	SWS01 sp3	
W33A[l]		18 14 39.44	−17 52 01.3		High	1.92	32900920	SWS01 sp4	
GL 7009S[l]		18 34 20.91	−05 59 42.2		High	2.52	15201140	SWS01 sp3	
GL 2136[l]		18 22 26.32	−13 30 08.2		High	1.48	33000222	SWS01 sp3	
S140 IRS 1[l]		22 19 18.17	+63 18 47.6		High	1.57	22002135	SWS01 sp4	
NGC 7538 IRS 9[l]		23 14 01.63	+61 27 20.2		High	2.31	09801532	SWS01 sp2	
Elias 16[m]		04 39 38.88	+26 11 26.6	Taurus	bg	...	0005637632	SL, SH	
EC 118[m]	CK 2	18 30 00.62	+01 15 20.1	Serpens	bg	...	0011828224	SL, SH	

NOTE.—Units of right ascension are hours, minutes, and seconds, and units of declination are degrees, arcminutes, and arcseconds.

[a] Position used in *Spitzer* IRS observations.

[b] Source type: Low = low mass YSO; High = massive YSO; bg = background star.

[c] Broadband spectral index as defined in eq. (1).

[d] AOR key for *Spitzer* and TDT number for *ISO* observations.

[e] *Spitzer* IRS modules used: SL = Short-Low (5–14 μm, $R \sim 100$), LL = Long-Low (14–34 μm, $R \sim 100$), SH = Short-High (10–20 μm, $R \sim 600$), LH = Long-High (20–34 μm, $R \sim 600$); *ISO* SWS modes used (2.3–40 μm): SWS01 speed 1 ($R \sim 250$), speed 2 ($R \sim 250$), speed 3 ($R \sim 400$), speed 4 ($R \sim 800$).

[f] Complementary ground-based L-band observations with Keck NIRSPEC or VLT ISAAC.

[g] Spectral index α enhanced due to foreground extinction. Exclusion of K_s band flux gives much lower α: −0.16 (Elias 29), −0.02 (B5 IRS 1), 0.18 (B5 IRS 3), and 0.38 (EC 82).

[h] Published previously in Boogert et al. (2004).

[i] Published previously in Watson et al. (2004).

[j] Published previously in Boogert et al. (2000a).

[k] Published previously in Pontoppidan et al. (2005).

[l] Published previously in Keane et al. (2001b).

[m] Published previously in Knez et al. (2005).

including all photometry (F_λ) available between the $\lambda = 2.17$ μm K_s band from the Two Micron All Sky Survey (2MASS; Skrutskie et al. 2006) and the $\lambda = 24$ μm *Spitzer* MIPS band. In the infrared broadband classification scheme (Wilking et al. 2001), most objects (35 out of 41) fall in the embedded Class 0/I category ($\alpha > 0.3$). The remaining 6 objects are Flat-type objects ($-0.3 < \alpha < 0.3$; Greene et al. 1994). Although most objects fall in the Class 0/I category, the dispersion within it is large. Some objects are envelope-dominated Class 0 sources undetected in the 2MASS K_s band (e.g., L1455 SMM 1, B1-c), while others are more likely to be Flat-type sources with dispersed envelopes and/or face-on disks extincted by foreground dust. The latter sources were identified by excluding the K_s band flux in the α determination and are marked as such in Table 1. Thus, our sample represents a wide range of YSO evolutionary stages and probably source orientation.

To contrast the possibly processed ices toward YSOs with ices toward quiescent regions, published mid-infrared spectra of two background stars toward the Serpens and Taurus clouds were included in the analysis (Knez et al. 2005). In addition, eight massive YSOs and two low-mass YSOs observed with the *ISO* satellite were included in the sample (Table 1). These serve as a reference in the ice feature analysis because their mid-infrared spectra are well studied at higher spectral resolution than is possible with *Spitzer* IRS and because the massive YSOs may trace different physical conditions that may affect the formation and evolution of the ices.

3. OBSERVATIONS AND DATA REDUCTION

Spitzer IRS spectra were obtained as part of the c2d Legacy program (PIDs 172 and 179), as well as a dedicated open time program (PID 20604). In addition, several previously published GTO spectra were included (Watson et al. 2004). The coordinates and IRS modules that were used for each source are listed in Table 1. For all modules the two-dimensional basic calibrated data (BCD) spectral images produced by the SSC pipeline version S13.2.0 or later were used as the starting point of the reduction. The low-resolution "Short-Low" and "Long-Low" modules (SL and LL; $R = \lambda/\Delta\lambda = 60$–$120$) were reduced in a way that is customary for ground-based spectra. First, the spectral and spatial dimensions were orthogonalized, and then the two-dimensional images of the two nodding positions were subtracted in order to remove extended emission. In some cases the background emission is highly structured or multiple sources are present in the slit, and instead of subtracting nodding pairs, the background emission was determined from neighboring columns in the extraction process. A fixed width extraction was performed and the one-dimensional spectra were then averaged. Subsequently, the spectra were divided by spectra of the standard stars HR 2194 (A0 V; PID 1417; AOR keys 0013024512 and 0013024768 for SL1 and SL2, respectively) and HR 6606 (G9 III; PID 1421; AOR key 0013731840 for LL) reduced in the same way in order to correct for wavelength-dependent slit losses. Spectral features were divided out using the photospheric models of Decin et al. (2004). The high-resolution "Short-High" and "Long-High" modules (SH and LH; $R \sim 600$) were reduced using the c2d pipeline (Lahuis 2007, pp. 25–52). An important difference with the low-resolution modules is the need for the removal of spectral fringes, which is done in the c2d pipeline as well. Many of the *Spitzer* spectra were complemented by ground-based Keck NIRSPEC (McLean et al. 1998) and VLT ISAAC (Moorwood 1997) L-band spectra at resolving powers of $R = 2000$ and 600, respectively. These were reduced in a way standard for ground-based long-slit spectra. Finally, the *Spitzer* IRS modules and ground-based spectra were multiplied along the flux scale in order to match *Spitzer* IRAC 3.6, 4.5, 5.8, and 8.0 μm and *Spitzer* MIPS 24 μm photometry (Evans et al. 2007), using the appropriate filter profiles.

For the *ISO* SWS satellite spectra used in this paper, the latest SPD pipeline version 10.1 products were taken from the *ISO* archive and the detector scans were cleaned from cosmic-ray hits and averaged. The final spectra do not show any significant differences with respect to the data published in Keane et al. (2001b).

4. RESULTS

All sources in the sample show numerous absorption features on top of rising, flat, or falling 2–35 μm SEDs (Fig. 1). Most of these features are due to ices (§ 4.2), and they are often accompanied by strong 9.7 μm and weaker 18 μm silicate absorption bands; but toward some sources, the silicate bands are in emission (e.g., RNO 15, IRAS 17081−2721). Also, prominent narrow emission lines of H_2 (S[5], S[6], and S[7]) are observed toward IRAS 03271+3013, CrA IRAS 32, and L1455 SMM 1. These belong to the most deeply embedded objects ($\alpha > 2$; Table 1) in the sample, and the line emission is most likely related to molecular outflow activity (e.g., Noriega-Crespo et al. 2004; Neufeld et al. 2006). CrA IRAS 32 shows the shock-related 5.340 μm emission line of Fe^+ (Neufeld et al. 2006) and a strong line at 6.628 μm, perhaps also due to Fe^+. These emission lines are not further analyzed here, but their presence compromises the analysis of the underlying absorption features in these particular sources. H I emission lines (most notably Brα at 4.052 μm and Pfγ at 3.740 μm) are present in many of the ground-based L-band spectra, but at the high spectral resolution contamination with the ice absorption features is not a problem. In sources with strong L-band H I emission (e.g., RNO 91) the blended Pfα (7.459 μm) and Huβ (7.502 μm) lines are weakly visible in the IRS spectra ($\sim$3% of the continuum), affecting the continuum determination for the low-contrast ice features in that region (§ 4.2; Öberg et al. 2008).

4.1. *Continuum Determination*

Determining the baseline for the absorption features in the spectra of embedded protostars is not trivial. The continuum SED underlying the many blended absorption features originates from warm dust near the central star and is dependent on poorly characterized parameters such as disk and envelope mass, size, and inclination and dust composition (Whitney et al. 2003). The continuum applied to each source and indicated in Figure 1 was derived as follows. Shortward of 5 μm the continuum is much better defined than at longer wavelengths, and therefore the 2–5 and 5–35 μm regions are treated separately. For the short-wavelength part, continuum points selected at 2.3, 3.9, and 5.0 μm are interpolated with a smooth spline function. Inclusion of the 2.3 μm portion of the spectrum, or K_s-band photometry, is essential in choosing the best continuum for the 3.0 μm absorption band. The continuum longward of 5 μm is much less constrained because the entire 5–32 μm region is covered by absorption features. Even the "emission peak" at 8.0 μm is covered by the long-wavelength wing of the 6.0 μm H_2O ice absorption band (e.g., Hudgins et al. 1993) and the short-wavelength wing of the 9.7 μm silicate band. The latter often extends toward shorter wavelengths compared to the silicate spectrum observed in the diffuse medium (e.g., toward GCS 3; Kemper et al. 2004). Some sources also show an additional depression at 8 μm due to yet unknown species; the best known example of this is the massive YSO W33A (Keane et al. 2001b; Gibb & Whittet 2002). Thus, an interpolation over a large wavelength range is required, with few constraints. When possible, a low-order polynomial [on a log (λF_λ) vs. log λ

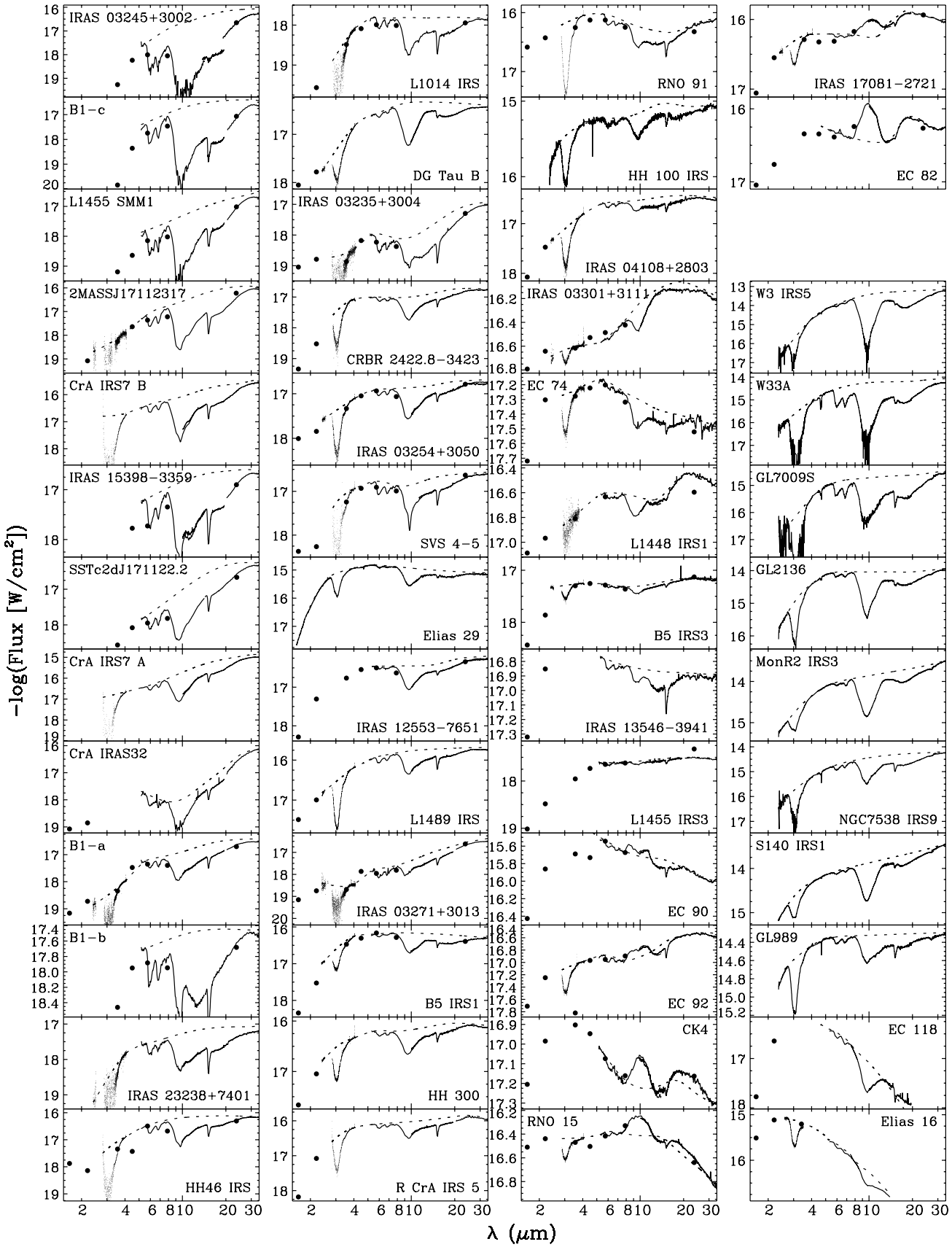

FIG. 1.— Observed *Spitzer* IRS and complementary *ISO* SWS and ground-based *L*-band spectra and the adopted continua (*dotted lines*). The large filled circles represent 2MASS and *Spitzer* IRAC and MIPS photometry from the c2d catalogs (Evans et al. 2007). Sources are ordered from top to bottom and left to right in decreasing 9.7 μm absorption band depth. Massive YSOs and background stars are separated in the right column below the white space.

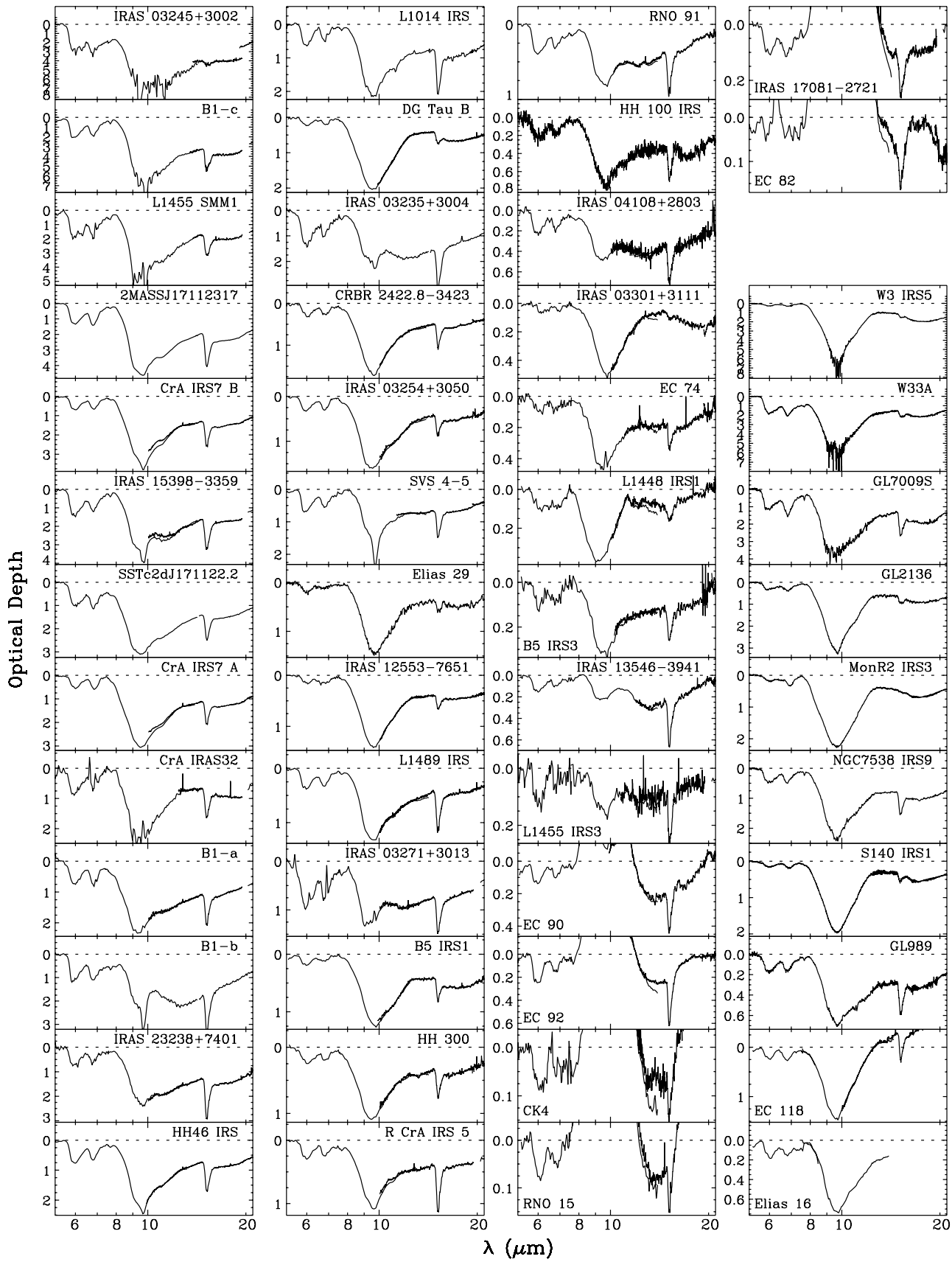

FIG. 2.— Optical depth 5–20 μm spectra, ordered from top to bottom and left to right in decreasing 9.7 μm absorption band depth. The horizontal dotted line indicates zero optical depth for reference. Massive YSOs and background stars are separated in the right column below the white space.

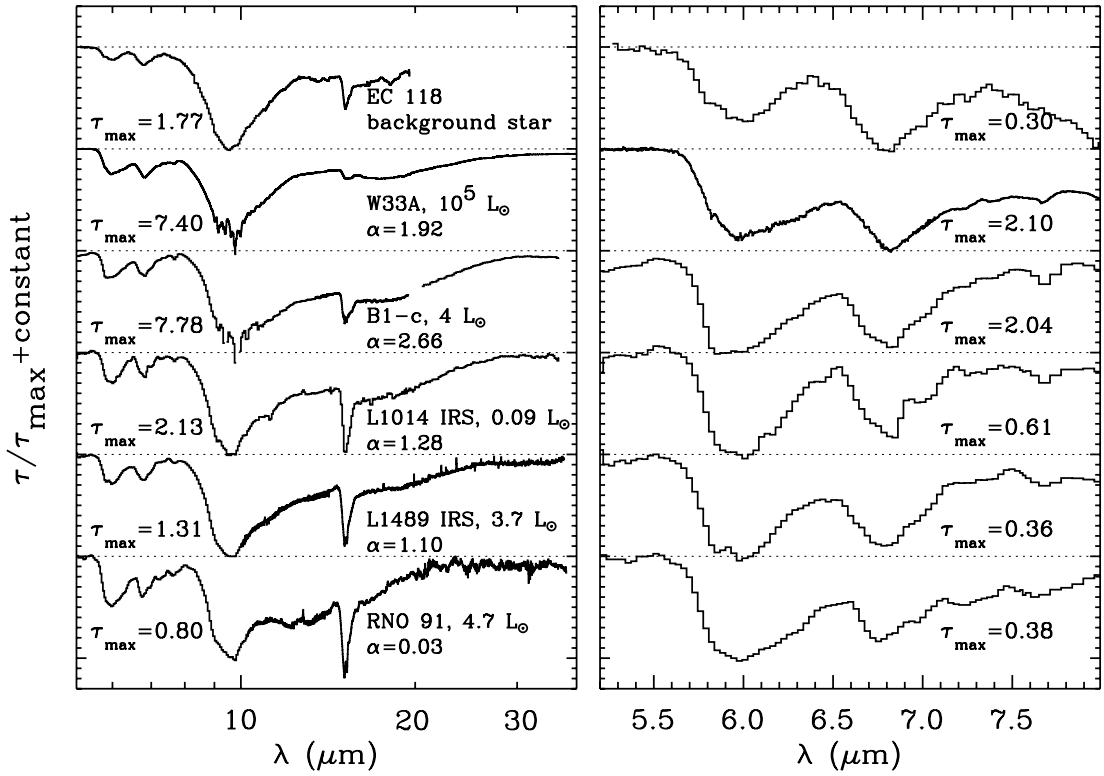

FIG. 3.—Optical depth spectra between wavelengths of 5.2–38 μm (*left*) and 5.2–8.0 μm (*right*) of a wide variety of sight lines. *Top to bottom*: EC 118, a background star behind the Serpens cloud (Knez et al. 2005); W33A, a massive YSO (Keane et al. 2001b); and the low-mass YSOs B1-c in the Perseus cloud, L1014 IRS in the isolated core L1014, L1489 IRS in the Taurus cloud, and RNO 91 in the L43 core near the Ophiuchus cloud. The low-mass YSOs are ordered from top to bottom in decreasing 2–25 μm SED spectral index α (eq. [1]) as indicated in the left panel. Also indicated is the bolometric luminosity. The spectra are scaled to the peak optical depth τ_{max} in the plotted range indicated near each spectrum. Note that despite the very different nature of the sight lines, the same ice absorption features are observed, although the shapes and depths vary from source to source.

scale] was used to interpolate between the 5 and 32 μm continuum points. This works best for the most deeply embedded sources (e.g., B1-c, 2MASS J17112317). For many sources, some guidance for the polynomial fit is provided by scaling the silicate spectrum of the diffuse medium source GCS 3 (Kemper et al. 2004) to the peak optical depth at 9.7 μm and by scaling a laboratory H_2O ice spectrum to the 3.0 μm band. Less embedded sources, i.e., the sources with relatively strong near-infrared emission (e.g., RNO 91, IRAS 03235+3004), show a decreasing continuum between 5 and 10 μm and an emission bump at longer wavelengths. Here a best effort spline continuum was defined, guided by modified blackbody curves below 10 μm. For the background stars the optical depth spectra presented in Knez et al. (2005) were used.

4.2. *Absorption Features*

The derived continua were used to put the spectra on an optical depth scale for the analysis of the wealth of absorption features (Figs. 1 and 2). The well-known 6.0 and 6.85 μm bands (e.g., Keane et al. 2001b) are detected in all sources, along with the 9.7 μm band of silicates (in either absorption or emission) and the 3.0 μm H_2O and 15 μm CO_2 ice bands when available. A number of weaker ice features (7.25, 7.40, 7.67, 9.0, and 9.7 μm) are detected in several sources as well. Examples in Figure 3 show that these same absorption features are present in sources of a very different nature (background stars, massive YSOs, Class 0, I, and flat-spectrum low-mass YSOs), but that the depths and the profiles vary. Very deep 6.0 and 6.8 μm bands, with peak optical depths of up to 2, are observed in the Class 0 sources. These are the deepest ice bands ever detected in low-mass YSOs, comparable to the most obscured massive YSOs (e.g., W33A, GL 7009S).

4.2.1. *The* H_2O *Ice Column Density*

H_2O is the most abundant molecule in interstellar ices (e.g., Keane et al. 2001b; Gibb et al. 2004), and strong, broad absorption bands are present over much of the observed spectral range: the O—H stretching mode between ~2.7 and 3.6 μm, the O—H bending mode between ~5.4 and 9 μm, and the libration mode between ~10 and 30 μm. Many absorption features of other species overlap with these H_2O bands, especially in the 5–8 μm region (§ 4.2.2), and in order to separate them, accurate (10%–20%) solid H_2O column densities are required. The 3.0 μm band provides, in principle, the most accurate H_2O column density because the O—H stretching mode is very strong and dominates over other species (Tielens et al. 1984). Evidently, the ice band must not be saturated, the continuum signal-to-noise ratio values must be sufficient, and photometry must be available below the 2.8 μm atmospheric gap for an accurate continuum determination (§ 4.1). None of these requirements are met for the most embedded objects in our sample (e.g., B1-c, 2MASS J17112317−2724315). For sources that do meet the requirements, the long-wavelength wing that often accompanies the 3.0 μm band is not taken into account in the H_2O column determination. The width of a laboratory pure H_2O absorption spectrum at the best-fitting temperature is assumed (Hudgins et al. 1993), using the integrated band strength $A = 2.0 \times 10^{-16}$ cm molecule^{-1} (Hagen et al. 1981). Thus, the calculated column density represents that of absorption by pure H_2O on small grains. If the wing were taken into account, the H_2O column density would be larger by at most 15% in some sources.

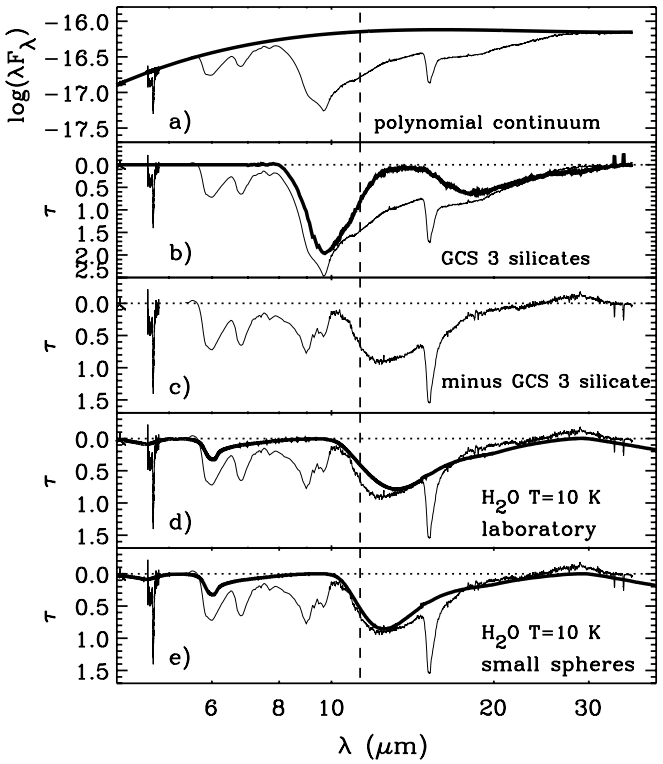

FIG. 4.—Proof of the presence of the 13 μm solid H_2O libration mode in the source HH 46 IRS. Panel (*a*) shows a smooth, unbiased polynomial continuum (*thick line*). The optical depth spectrum is compared to the silicate spectrum of the GC source GCS 3 in (*b*) (*thick line*; Kemper et al. 2004). After subtracting GCS 3, a prominent absorption feature is found at 10–20 μm that is likely due to the strong libration mode of H_2O (panel [*c*]), as is shown by a comparison to a laboratory spectrum of pure amorphous H_2O ice at $T = 10$ K (*thick line*; panel [*d*]). This band is particularly sensitive to grain shape effects, and a better fit is obtained with small spherical grains (*thick line*; panel [*e*]). The column densities of H_2O derived from the 3 and 13 μm bands are in good agreement, further validating the correctness of the applied method. The vertical dashed line is the 11.3 μm absorption feature presented in Boogert & Ehrenfreund (2004) and Kessler-Silacci et al. (2005).

The wing, which has an integrated optical depth of at most 30% with respect to the rest of the 3 μm band, is probably caused by a combination of scattering on large ice-coated grains (radius >0.5 μm) and absorption by ammonia hydrates (Hagen et al. 1983; Dartois & d'Hendecourt 2001). Only the former would contribute to the H_2O column density, but less than expected for small grains because the integrated extinction (absorption+scattering) strength per molecule is a factor of 2 larger for large grains than it is for small grains (e.g., Fig. 7 in Dartois & d'Hendecourt 2001).

An alternative, and sometimes the only, way to determine the H_2O column density is by measuring the peak strength of the libration mode in the 11–14 μm region. This band is difficult to isolate in the spectrum because it is several microns wide and wedged between the strong 9.7 and 18 μm silicate features. However, application of a low-order polynomial continuum to HH 46 IRS (Fig. 4) and subtraction of a standard interstellar silicate spectrum (GCS 3; Kemper et al. 2004) show a broad feature centered on ~12.3 μm that is attributed to the H_2O libration mode. Using a laboratory spectrum of a thin film of pure H_2O ice at $T = 10$ K (Hudgins et al. 1993), the depth is in good agreement with the 3.0 μm stretching mode, but there is a discrepancy in the peak position by about 1 μm (Fig. 4). The peak position of the libration mode is quite sensitive to the shape of the grains, and for small spherical grains (using the formulation of Bohren & Huffman 1983) a much better calculated fit is obtained (Fig. 4). At such large shift to shorter wavelengths, the H_2O libration mode overlaps with the steep edge of the 9.7 μm silicate band and a substructure is introduced reminiscent of the 11.3 μm absorption feature reported in Boogert et al. (2004) and Kessler-Silacci et al. (2005). Finally, this method of determining the H_2O column density works well for deeply embedded sources (Fig. 5), but it fails when a silicate emission component is present, filling in the H_2O absorption (e.g., RNO 91).

4.2.2. *The* 5–8 μm *Absorption Complex*

Prominent absorption bands are present at 6.0 and 6.8 μm in all sources. In between these bands (~6.5 μm), the optical depth is nonzero and varies relative to the 6.0 and 6.8 μm peak optical depths for different sources (e.g., Fig. 3). Beyond 7.0 μm, "featureless" absorption is present up to 8 μm that approaches zero optical depth at 8 μm in some sources, but continues to be significant in others and merges with the 9.7 μm silicate band. Here an attempt is made to decompose this complex blend of absorption features. Distinct, much weaker bands that are present in a subset of sources at 7.25, 7.4, and 7.6 μm are discussed separately (§ 4.2.3).

Solid H_2O is a major contributor to the optical depth in the 5–8 μm region by its O—H bending mode at 6.0 μm and the overtone of the libration mode extending between 6 and 8 μm (e.g., Devlin et al. 2001). For consistency with previous work, although formally incorrect, these overlapping bands will be referred to as a single mode, the O—H bending mode of H_2O. Its absorption profile depends on the ice structure. In particular, as an amorphous ice is heated from $T = 10$ to 80 K, the distinct peak at 6.0 μm becomes weaker (Hudgins et al. 1993; Maldoni et al. 1998). At higher temperatures, the shape remains relatively constant. For almost half of the sample the ice temperature could be determined from the shape of the 3.0 μm H_2O stretching mode (Table 2). Most other YSOs are deeply embedded, and $T = 10$ K was assumed. Subsequently, a laboratory spectrum of pure H_2O (Hudgins et al. 1993) at the determined temperature was scaled to the column density derived from the 3.0 and 13 μm bands (§ 4.2.1) and subtracted from each optical depth spectrum. The shapes and depths of the residual features, and any variations thereof between sources, are analyzed. It should be kept in mind, however, that some features may still be the result of interactions of species with H_2O in solid-state matrices, such as the narrow peak induced in H_2O:CO_2 mixtures (§ 6.3; Knez et al. 2005; Öberg et al. 2007).

Toward most low-mass YSOs, the observed 6.0 μm absorption band is deeper than expected from the 3.0 and 13 μm H_2O ice bands (Fig. 6). Such a discrepancy has been reported toward massive YSOs as well (Cox 1989; Schutte et al. 1996; Gibb et al. 2000; Keane et al. 2001b), and it is quantified in units of the H_2O column density as follows:

$$E_6 = \frac{\int_{1562}^{1785} \tau_\nu \, d\nu}{N(\mathrm{H_2O})(1.2 \times 10^{-17})0.60}, \qquad (2)$$

which is the integrated optical depth of the 6.0 μm band in wavenumber (ν) space divided by the H_2O column density derived from the 3.0 and/or 13 μm bands. The factor of 1.2×10^{-17} is the integrated band strength of the O—H bending mode in a pure H_2O laboratory ice (Gerakines et al. 1995) in units of cm molecule^{-1}. The latter extends all the way out to 8.5 μm, while the numerator of equation (2) integrates only to 6.4 μm. Therefore, the laboratory band strength is reduced by a factor of 0.60, as derived from the laboratory spectra. E_6 varies significantly: from ≥ 2 in

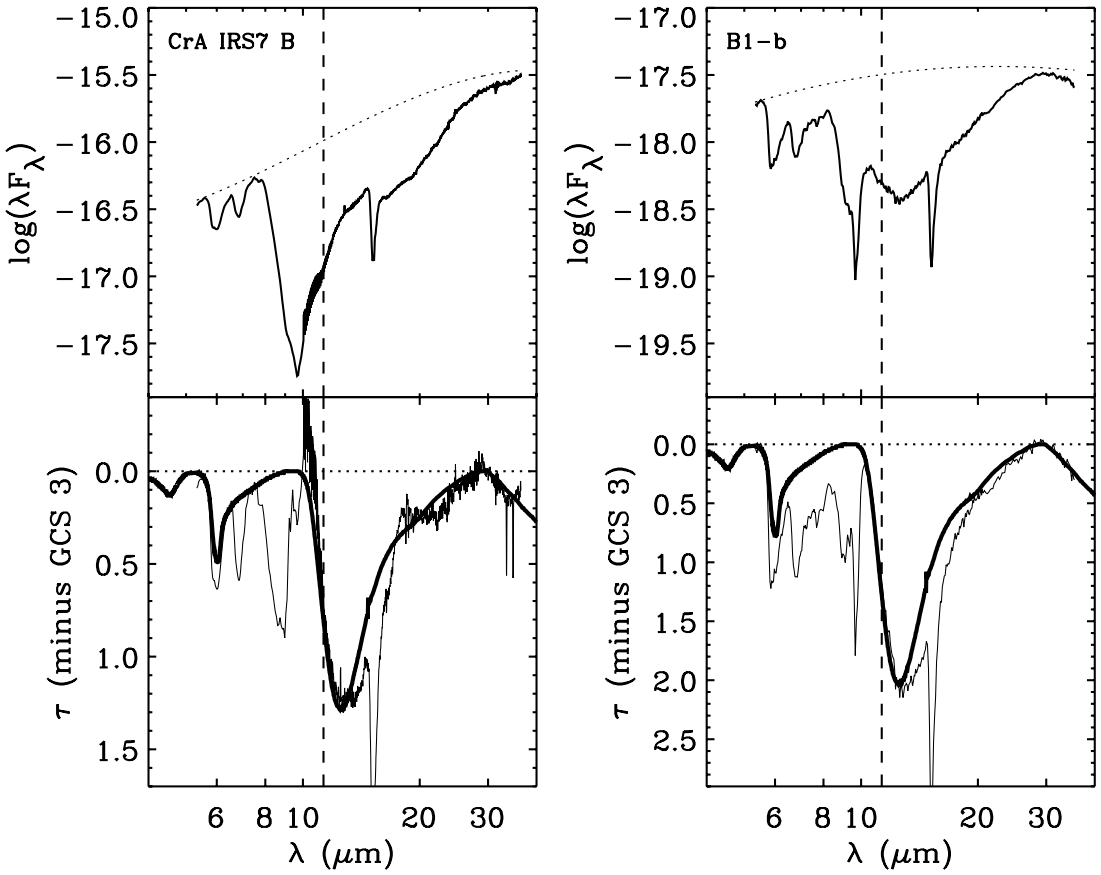

FIG. 5.—In deeply embedded sources the 13 μm H_2O libration mode can be used to reliably measure the solid H_2O column density. "Silicate-free" optical depth spectra were derived in the same way as shown in Fig. 4 for the YSOs CrA IRS 7 B (*left*) and B1-b (*right*). For each source the top panel shows the observed spectrum and the polynomial continuum (*dotted line*), and the bottom panel the optical depth spectrum. Note the very prominent libration mode and the peculiar absence of silicates toward B1-b. Again, small spherical grains of pure H_2O at $T = 10$ K (*thick line*) fit the peak position of the observed band well, although excess absorption is visible on the long-wavelength side. Finally, note that the downturn above 30 μm is likely real and due to the onset of the H_2O lattice mode, as the good fits with the laboratory data show.

~30% of the YSOs (e.g., RNO 91, IRAS 03301+3111, EC 92) to 1.0 (i.e., no excess) in other YSOs (Table 2 and Fig. 7).

The large source-to-source variations of E_6 may hold clues to the nature of the carrier(s) of the 6.0 μm excess absorption. As is illustrated in Figure 8, these variations are used to separate any independent, overlapping absorption components in the 5–8 μm range. Initially, a selection of sources with low values of E_6 and sources with high values of E_6 is averaged, and the resulting spectra are scaled and subtracted from each other such that the distinct peak at 6.85 μm is removed. What remains is a very broad feature, stretching between 5.8 and 8 μm. While the profiles of the 6.0 and 6.85 μm bands themselves look rather similar for many sources (e.g., like HH 46 IRS), significant source-to-source variations are sometimes observed (Fig. 9). The peak position of the

TABLE 2
FIT PARAMETERS

Source	T_{H_2O}[a]	E_6[b]	$\tau_{9.7}$[c]	$\tau_{6.0}$[d]	τ_{C1}[e]	τ_{C2}[f]	τ_{C3}[g]	τ_{C4}[h]	τ_{C5}[i]
L1448 IRS 1	10	4.35 (1.57)	0.36 (0.04)	0.10 (0.01)	0.00 (0.01)	0.00 (0.01)	0.02 (0.01)	0.03 (0.01)	0.08 (0.01)
L1489 IRS.....	40*	1.77 (0.21)	1.32 (0.13)	0.37 (0.02)	0.15 (0.06)	0.05 (0.06)	0.19 (0.02)	0.08 (0.02)	0.06 (0.02)
HH 46 IRS.....	40	2.00 (0.20)	2.23 (0.22)	0.75 (0.04)	0.34 (0.13)	0.17 (0.13)	0.36 (0.02)	0.18 (0.02)	0.10 (0.02)
RNO 91.....	40*	1.99 (0.17)	0.80 (0.08)	0.39 (0.02)	0.13 (0.05)	0.07 (0.05)	0.13 (0.01)	0.06 (0.01)	0.10 (0.02)
W33A.....	40	2.57 (0.64)	6.02 (0.60)	1.87 (0.03)	0.46 (0.20)	0.28 (0.20)	0.74 (0.05)	0.51 (0.05)	0.67 (0.07)

NOTES.—Uncertainties in parentheses based on statistical errors in the spectra only, unless noted otherwise below. Table 2 is published in its entirety in the electronic edition of the *Astrophysical Journal*. A portion is shown here for guidance regarding its form and content.

[a] Temperature of pure H_2O laboratory ice (Hudgins et al. 1993) assumed. Values indicated with an asterisk are most accurate because of the availability of good-quality *L*-band spectra.

[b] The 6.0 μm excess as defined in eq. (2). Uncertainty includes uncertainty in $N(H_2O)$.

[c] Peak optical depth at 9.7 μm, without correction for underlying emission. Uncertainty includes 10% of $\tau_{9.7}$ to account for errors in the continuum determination.

[d] Peak optical depth at 6.0 μm, including H_2O absorption.

[e] Peak optical depth component C1.

[f] Peak optical depth component C2.

[g] Peak optical depth component C3.

[h] Peak optical depth component C4.

[i] Peak optical depth component C5. Uncertainty includes uncertainty in $N(H_2O)$ as this affects the baseline level. The continuum uncertainty is not included. It is likely on the order of 0.03 for most sources.

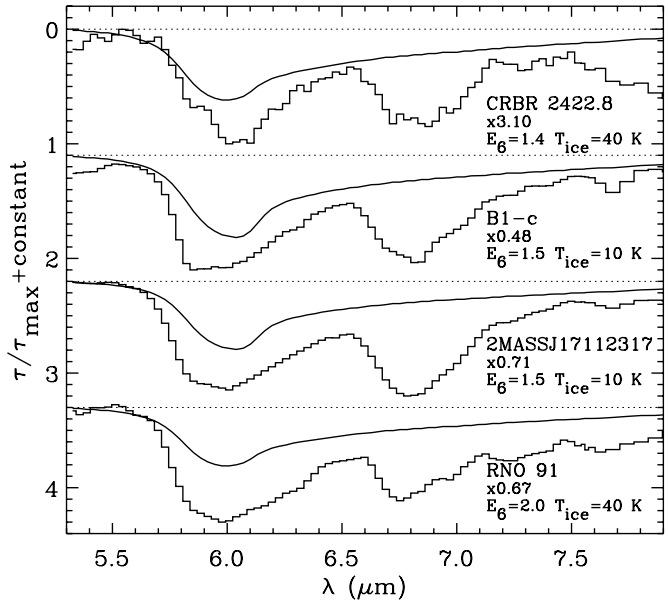

FIG. 6.—Selection of 5–8 μm spectra of four low-mass YSOs on normalized optical depth scales (*solid histogram*). The normalization factors are indicated for each source. The smooth solid line represents a laboratory spectrum of pure, amorphous solid H_2O at the indicated temperature at the column density derived from the 3.0 and 13 μm bands. Clearly, in all sources a significant fraction of the absorption is not explained by solid H_2O, and it varies from source to source. For the 6.0 μm feature this fraction is indicated by the value of E_6, defined in eq. (2). Note the variations of the profiles of the 6.0 and 6.85 μm bands, as well as the presence of weak features at 7.25, 7.4, and 7.65 μm.

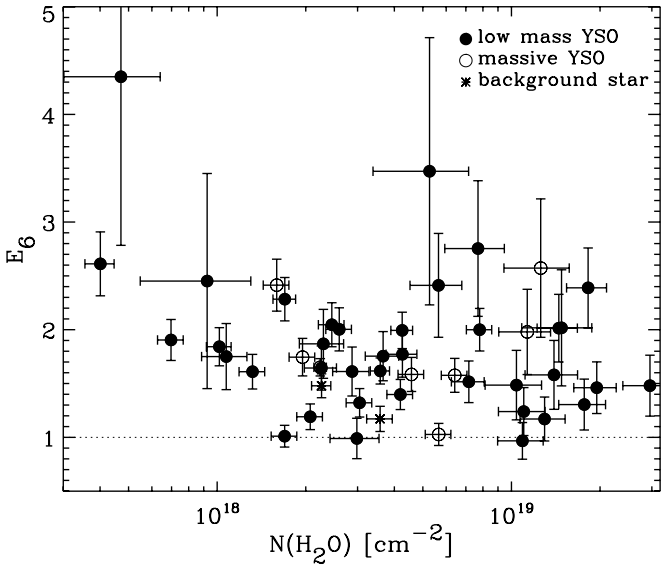

FIG. 7.—Values of E_6 (defined in eq. [2]) plotted as a function of the solid H_2O column density for the entire source sample: low-mass YSOs (*filled circles*), massive YSOs (*open circles*), and background stars (*asterisks*). For sources near the horizontal dotted line the entire 6.0 μm absorption band can be explained by pure H_2O ice. All other sources have significantly deeper 6.0 μm bands than expected from the 3 or 13 μm bands.

6.0 μm component varies between 5.85 and 6.2 μm and broadens as the feature shifts toward longer wavelengths. At the same time the 6.85 μm band shifts from 6.8 to 6.95 μm. By subtracting extreme spectra from each other, it is found that the latter consists of two components centered at 6.755 and 6.943 μm with widths of FWHM = 0.195 and 0.292 μm, respectively, similar to what was previously found for massive protostars (Keane et al. 2001b). The 6.0 μm band consists of two components as well, with peak positions of 5.84 and 6.18 μm and FWHM widths of 0.26 and 0.40 μm, respectively.

It is thus hypothesized that, after H_2O subtraction, the 5–8 μm absorption in all sources is composed of five distinct components (Fig. 8): a set of bands peaking at 5.84 and 6.18 μm (C1 and C2 hereafter), a set of bands peaking at 6.755 and 6.943 μm (C3 and C4), and a broad asymmetric feature stretching between 5.8 and 8 μm and peaking near 5.9 μm (C5). Example fits with these components are shown in Figure 10. The peak optical depths of the components in all sources are listed in Table 2. The indicated error bars are based on statistical uncertainties in the spectral data points, except for C5. The accuracy of the C5 optical depth is affected by the accuracy of the baseline, which at present can only partly be quantified. The baseline uncertainty is a combination of the error in $N(H_2O)$ (Table 3) and the poorly known error in the continuum choice (§ 4.1). For many sources the latter, not included in Table 2, is likely at most 0.03 on optical depth scale.

4.2.3. *Weak Features in the* 7–8 μm *Wavelength Range*

In addition to solid H_2O and the five components discussed above, a number of weak features can be discerned in the 7–8 μm region of several low-mass YSOs, much like those identified toward massive protostars (Schutte et al. 1999). These features lie on top of a curved "continuum" created by the wings of the prominent 6 and 6.85 μm features. A high-order polynomial (up to sixth) had to be used to fit a local baseline to typically these wavelength regions: 7.00–7.14, 7.3–7.35, 7.47–7.50, and 7.80–7.95 μm. Examples of the resulting features are shown in Figure 11, where they are compared to the higher resolution (R = 800) *ISO* SWS spectrum of the massive YSO W33A. The 7.25 μm feature is likely due to the HCOOH molecule (§ 5.1.2). The feature at 7.40 μm is possibly due to $HCOO^-$ (§ 5.1.5; Schutte et al. 1999), while the 7.67 μm feature is identified with CH_4 (Boogert et al. 1996; Öberg et al. 2008).

4.2.4. *Substructures in the* 9.7 μm *Silicate Absorption Band*

Several sources show substructures at 9.0 and 9.7 μm within the strong silicate absorption band (Fig. 12). Previous work indicated that these can be attributed to the umbrella mode of solid NH_3 and the C—O stretching mode of CH_3OH (e.g., Lacy et al. 1998; Skinner et al. 1992). To extract these and any other ice absorption features in the 8–12 μm range, the silicate absorption and possible blended emission need to be accurately modeled. This is deferred to a future publication (S. Bottinelli 2008, in preparation), and here a local fourth-order polynomial continuum is fitted to the wavelength regions 8.25–8.75, 9.23–9.37, and 9.98–10.4 μm to extract the features (Fig. 12). Column densities of CH_3OH and NH_3 derived from these and other features are further discussed in §§ 5.1.1 and 5.1.4.

5. CONSTRAINING THE ORIGIN OF THE 5–8 μm ABSORPTION FEATURES

Numerous carriers have been proposed to account for the various features in the 5–8 μm wavelength region (Tielens et al. 1984; Keane et al. 2001b). Here new observational constraints to possible carriers are discussed, using the present large source sample and wavelength coverage. First, the contributions of the most securely identified (CH_3OH, NH_3) or otherwise well-constrained species (H_2CO, HCOOH, $HCOO^-$) to the observed C1–C5 components are discussed (§ 5.1). Subsequently, the origin of the remaining absorption is constrained by correlating it with a number of other observables (§ 5.2).

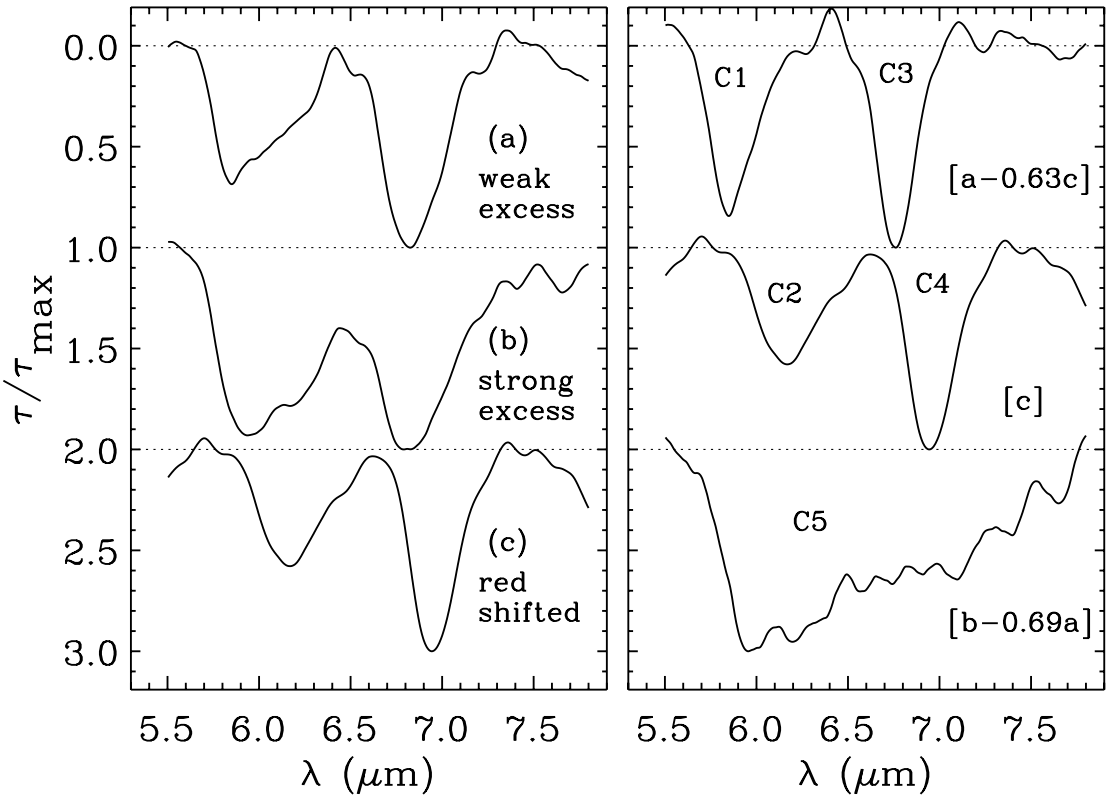

FIG. 8.—Demonstration of the decomposition of the 5–8 μm absorption complex. In the left panel are shown averaged, smoothed, H_2O-subtracted spectra of YSOs with small 6.0 μm excess (spectrum a), YSOs with strong 6.0 μm excess (spectrum b), and the YSO IRAS 03301+3111, which shows strongly redshifted 6.0 and 6.85 μm bands (spectrum c). Applying linear combinations of spectra a, b, and c in the left panel, five independent absorption components are found and shown in the right panel. Components C1 and C3 are found by subtracting spectrum c, multiplied by a factor of 0.63, from spectrum a (*top*). Components C2 and C4 are identical to spectrum c (*middle*). Component C5 is found by subtracting spectrum a, multiplied by a factor of 0.69, from spectrum b (*bottom*). These five components, in addition to the bending mode of H_2O, are responsible for the 5–8 μm absorption complex in YSOs and background stars. Example fits are shown in Fig. 10. Note that C3 and C4 are the previously found short- and long-wavelength components of the 6.85 μm band (Keane et al. 2001b).

5.1. *Absorption by Known Species*

5.1.1. CH_3OH

Solid CH_3OH was previously unambiguously detected by its C−H stretching mode at 3.54 μm (e.g., Grim et al. 1991) and its C−O stretching mode at 9.7 μm (Skinner et al. 1992). In our sample, a Gaussian was fitted to the 9.7 μm feature on an optical depth scale and a CH_3OH detection is claimed if the integrated optical depth has a larger than 3 σ significance and if the peak position and FWHM are similar to previous detections, i.e., within 9.68–9.76 and 0.25–0.36 μm, respectively. The 3.54 μm band, when available, was treated similarly. Thus, CH_3OH was positively identified in 12 low-mass YSOs (Table 3; Fig. 13). Of those, 6 are based on the 9.7 μm band only. Column densities were calculated using integrated band strengths of 5.6×10^{-18} and 1.6×10^{-17} cm molecule^{-1} for the 3.54 and 9.7 μm bands, respectively (Kerkhof et al. 1999). In agreement with previous studies (Dartois et al. 1999; Pontoppidan et al. 2003a), the CH_3OH column varies considerably with respect to solid H_2O: from low upper limits of a few percent (3 σ) in several sources to detections of up to 30% in a few others. In the 5–8 μm region, the C−H deformation mode of CH_3OH overlaps with the C3 component and, at the derived column densities, contributes typically 5%–20% to its strength, but up to 40% for SVS 4-5 and GL 7009S.

5.1.2. HCOOH

The main vibrational modes of formic acid (HCOOH) occur in the 3–4 μm region (O−H and C−H stretch), at 5.85 μm (C=O stretch), at 7.25 μm (C−H deformation), and at 8.1 μm (C−O stretch). Previously, the 7.25 μm band was detected toward massive YSOs, while the 5.85 μm band, in addition to H_2O, could explain most of the 6 μm absorption (Schutte et al. 1999). The 7.25 μm band offers the most secure identification, even though its intrinsic strength ($A = 2.6 \times 10^{-18}$ cm molecule^{-1}) is a factor of ~25 weaker than the 5.85 μm band. It is least blended with other features and is unambiguously detected ($\geq 3\,\sigma$) toward nine low-mass YSOs (Fig. 11; Table 3). With the aid of laboratory analogs (Bisschop et al. 2007), the observed strength of the 7.25 μm feature is used to determine the contribution of HCOOH to the 6.0 μm band. Pure HCOOH and mixtures with H_2O show 7.25 μm features that are at least a factor of 2 wider than the observed band (FWHM ~ 15 cm^{-1}) and that peak at too short wavelengths. Schutte et al. (1999) and recently Bisschop et al. (2007) note that the band narrows and shifts to longer wavelengths in tertiary mixtures, specifically in $H_2O : CH_3OH : HCOOH = 100 : 40 : 12$ (Fig. 14). Such a mixture would be consistent with the detections and upper limits of solid CH_3OH [typically $N(CH_3OH) > N(HCOOH)$ toward YSOs; Table 3]. For the purpose of this analysis the laboratory and interstellar data are matched by scaling their integrated 7.25 μm optical depths. For these sources, the HCOOH column densities are 1%–5% with respect to solid H_2O (Fig. 13) and 50%–100% of component C1 can be explained by the C=O stretching mode of HCOOH (Fig. 14). This wide range encompasses the large uncertainty in the band strength: the laboratory 5.85 μm band is stronger by 60% in H_2O mixtures compared to pure HCOOH. For many sources in which the 7.25 μm band is not detected ($<3\,\sigma$), a stronger constraint on the HCOOH column density is provided by the strength of the C1 feature. Relative

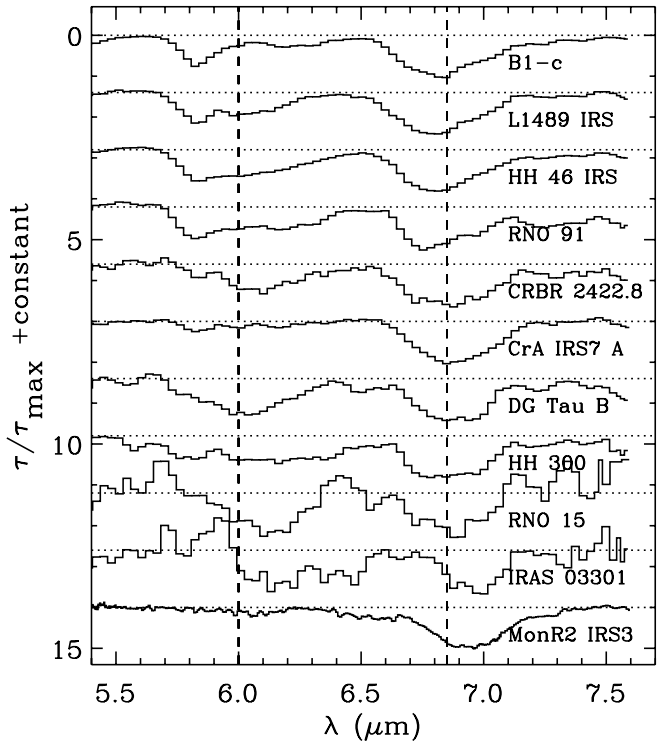

FIG. 9.—Residual absorption in the 5–8 μm region for a selection of sources, after subtraction of pure H_2O and component C5. The vertical dashed lines at 6.0 and 6.85 μm are plotted to facilitate comparing the positions of the features in the different sources. Note that the plotted sources represent the most extreme cases of our sample; most sources resemble the spectrum of HH 46 IRS. The spectra are normalized on optical depth scale and sorted from top to bottom in increasing wavelength of the 6 μm residual. Note that at the same time the 6.85 μm feature shifts to longer wavelengths as well.

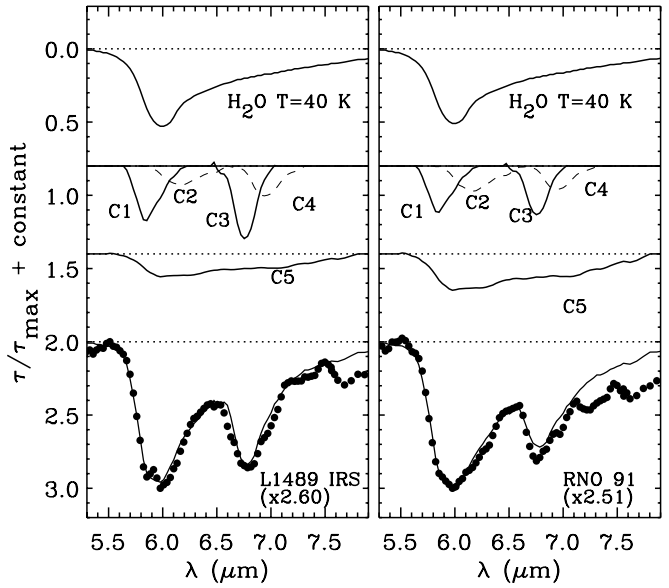

FIG. 10.—Examples of fits to the 5–8 μm absorption complex with the five components derived in Fig. 8, as well as H_2O. In the left and right panels two different YSOs are shown. The filled circles are the observed data points, and the thin line through them is the sum of all components above.

HCOOH abundances of a few percent are derived by using the C=O band strength of the H_2O-rich mixtures. Finally, in most cases neither the series of shallow, broad HCOOH bands in the 3–4 μm O−H and C−H stretching mode region nor a band at 8.1 μm, blended with the edge of the prominent 9.7 μm silicate feature, provide stronger constraints to the HCOOH column density.

5.1.3. H_2CO

As was noted for massive YSOs (e.g., Keane et al. 2001b), the C1 component shows a sharper edge on the short-wavelength side than can be explained by HCOOH alone. The C=O stretching mode of H_2CO is a viable candidate, and, assuming an integrated band strength of $A = 9.6 \times 10^{-18}$ cm molecule^{-1} (Schutte et al. 1993), substantially better fits to component C1 are obtained by adding typically an abundance of 6% of H_2CO with respect to H_2O (Fig. 15). Accurate H_2CO abundances and uncertainty estimates are hard to establish due to the strong blend with HCOOH. This abundance estimate is consistent with the nondetection of the C−H stretching bands at 3.34, 3.47, and 3.54 μm and leads to a contribution of 10%–35% from H_2CO to component C1. At the quoted typical abundance, the C−H bending mode vibration of H_2CO at 6.68 μm contributes $\leq$15% to component C3 (assuming $A = 3.9 \times 10^{-18}$ cm molecule^{-1} from Schutte et al. 1993).

5.1.4. NH_3

The abundance of solid NH_3 has long been a matter of debate because all of its absorption bands overlap with much stronger bands of H_2O and silicates. A combined in-depth analysis of all these features is therefore required, and accurate column densities will be presented elsewhere (S. Bottinelli et al. 2008, in preparation). In this work, NH_3 column densities accurate to within a factor of a few are sufficient. The strength of the 9.0 μm umbrella mode is used to calculate the strength of the 6.16 μm N−H bending mode and its contribution to component C2. The inflection seen at 9.0 μm in several sources is fitted with a Gaussian on optical depth scale, and a detection of NH_3 is claimed if the measured peak position and FWHM width are within 8.91–9.05 and 0.20–0.45 μm, respectively. Thus, NH_3 is positively identified in 17 low-mass YSOs. Column densities were calculated using an integrated band strength of 1.3×10^{-17} cm molecule^{-1} for NH_3 mixed in an H_2O ice (Kerkhof et al. 1999), leading to values of typically 3%–8% with respect to H_2O. At these abundances, 10%–50% of the C2 component is due to solid NH_3.

5.1.5. $HCOO^-$

The formate ion ($HCOO^-$) is an interesting candidate to consider because its C=O stretching mode at 6.33 μm overlaps with the C2 component, its C−H deformation mode coincides with the 7.40 μm band detected in several sight lines (Fig. 11), and it is chemically related to the HCOOH species discussed above (Schutte et al. 1999). Its identification is tentative, however, since acetaldehyde (CH_3HCO) has a feature at 7.40 μm as well, but not near the C2 component. If $HCOO^-$ were the carrier of the 7.40 μm band, its column density would be $\sim$0.3% with respect to solid H_2O, an order of magnitude less than HCOOH, and its contribution to component C2 would be $\leq$20%.

5.1.6. *Composite Laboratory Spectrum*

To illustrate that the independently derived column densities of solid HCOOH, $HCOO^-$, H_2CO, NH_3, and CH_3OH are indeed consistent with the 5–7 μm observations, laboratory spectra of these ices are scaled and subsequently added (Fig. 15). While no attempt is made to match the band profiles in detail (profiles are highly dependent on interactions in the ice matrix and a detailed analysis awaits further laboratory work), the agreement is encouraging. A considerable fraction of the interstellar 5–8 μm absorption consists of a complex blend of features from these simple ices. In particular, they explain most of the observed strength of component C1 (50%–100%), much of C2 (30%–70%), and some of

TABLE 3

COLUMN DENSITIES OF THE ICES

Source	$N(H_2O)$ (10^{18} cm^{-2})	N(HCOOH)[a] (% H_2O)	$N(CH_3OH)$ (% H_2O)	$N(NH_4^+)$[b] (% H_2O)
L1448 IRS 1	0.47 (0.16)	$\leq$12.1	$<$14.9	13.9 (4.6)
IRAS 03235+3004	14.48 (2.26)[c]	$\leq$2.7	4.2 (1.2)	2.2 (0.9)
IRAS 03245+3002	39.31 (5.65)[c]	$\leq$1.2	$<$9.8	5.5 (0.7)
L1455 SMM 1	18.21 (2.82)[c]	3.3 (0.8)	$<$13.5	7.1 (1.6)
RNO 15	0.69 (0.06)	$\leq$5.8	$<$5.0[d]	13.5 (2.4)
L1455 IRS 3	0.92 (0.37)[c]	$\leq$15.1	$<$12.5	8.9 (5.5)
IRAS 03254+3050	3.66 (0.47)	$\leq$3.2	$<$4.6	8.2 (1.1)
IRAS 03271+3013	7.69 (1.76)[c]	$\leq$2.5	$<$5.6	5.8 (3.3)
IRAS 03301+3111	0.40 (0.04)	$\leq$4.9	$<$15.1	8.1 (3.2)
B1-a	10.39 (2.26)[c]	$<$2.8	$<$1.9	7.7 (0.7)
B1-c	29.55 (5.65)[c]	1.2 (0.3)	$<$7.1	6.7 (0.3)
B1-b	17.67 (3.20)[c]	3.1 (0.5)	11.2 (0.7)	2.9 (0.4)
B5 IRS 3	1.01 (0.09)	$\leq$4.4	$<$8.1	15.3 (3.6)
B5 IRS 1[e]	2.26 (0.28)	$\leq$2.6	$<$3.7	5.2 (1.3)
L1489 IRS	4.26 (0.51)	$\leq$2.9	4.9 (1.5)[d]	6.2 (0.8)
IRAS 04108+2803	2.87 (0.40)	$\leq$3.1	$<$3.5	6.9 (0.9)
HH 300	2.59 (0.25)	$\leq$2.5	$<$6.7	5.5 (1.1)
DG Tau B	2.29 (0.39)	$\leq$3.4	$<$5.7	9.3 (1.8)
IRAS 08242$-$5050[e]	7.79 (0.77)[c]	2.7 (0.7)	5.5 (0.3)[d]	6.3 (0.4)
IRAS 12553$-$7651	2.98 (0.56)[c]	$\leq$1.8	$<$3.0	8.4 (2.1)
IRAS 13546$-$3941	2.07 (0.20)[c]	$<$8.3	$<$3.9	3.6 (0.7)
IRAS 15398$-$3359	14.79 (3.95)[c]	1.9 (0.3)	10.3 (0.8)	3.9 (0.3)
Elias 29[e]	3.04 (0.30)	$\leq$11.3	$<$4.9[d]	3.2 (1.0)
CRBR 2422.8$-$342[e]	4.19 (0.41)	$\leq$1.0	$<$9.3	6.7 (0.7)
RNO 91	4.25 (0.36)	$\leq$3.2	$<$5.6	5.4 (0.6)
IRAS 17081$-$2721	1.31 (0.13)	$\leq$2.4	3.3 (0.8)[d]	9.9 (1.8)
SSTc2d J171122.2$-$272602	13.94 (2.82)[c]	3.0 (0.6)	$<$1.3	6.4 (0.5)
2MASS J17112317$-$272431	19.49 (3.20)[c]	2.5 (0.5)	$<$3.2	6.7 (0.4)
EC 74	1.07 (0.18)	$\leq$3.2	$<$9.3[d]	9.7 (2.8)
EC 82[e]	0.39 (0.07)	$\leq$2.5	$<$14.2	10.2 (6.3)
SVS 4-5[e]	5.65 (1.13)	4.6 (1.0)	25.2 (3.5)[d]	3.6 (0.5)
EC 90[e]	1.69 (0.16)	$\leq$4.1	6.8 (1.6)	4.4 (0.9)
EC 92[e]	1.69 (0.14)	$\leq$5.3	11.7 (3.5)[d]	2.9 (1.8)
CK 4	$<$1.56	...	...	...
R CrA IRS 5	3.58 (0.26)	$\leq$4.1	6.6 (1.6)[d]	5.1 (0.4)
HH 100 IRS[e]	2.45 (0.24)	$\leq$2.4	$<$9.7[d]	11.6 (2.1)
CrA IRS 7A	10.89 (1.92)[c]	$\leq$0.6	$<$3.8	7.0 (0.4)
CrA IRS 7B	11.01 (1.97)[c]	$\leq$1.5	6.8 (0.3)	5.8 (0.2)
CrA IRAS 32	5.26 (1.88)[c]	$\leq$9.8	$<$18.1	15.9 (7.9)
L1014 IRS	7.16 (0.91)[c]	5.4 (1.3)	3.1 (0.8)	7.2 (1.0)
IRAS 23238+7401	12.95 (2.26)[c]	$\leq$1.5	$<$3.6	4.8 (0.7)
W33A[e]	12.57 (3.14)	5.2 (0.7)	14.7 (3.6)[d]	8.1 (0.8)
GL 2136[e]	4.57 (0.45)	5.1 (1.2)	8.5 (2.1)[d]	7.2 (0.9)
W3 IRS 5[e]	5.65 (0.56)	$\leq$0.4	$<$2.8[d]	7.0 (0.4)
S140 IRS 1[e]	1.95 (0.19)	$<$2.6	$<$3.0[d]	9.6 (1.0)
NGC 7538 IRS 9[e]	6.41 (0.64)	$<$2.0	7.5 (1.8)[d]	5.7 (0.4)
Mon R2 IRS 3[e]	1.59 (0.15)	$\leq$2.7	$<$5.6[d]	25.9 (2.2)
GL 989[e]	2.24 (0.10)	$\leq$2.2	3.1 (0.1)	8.4 (0.7)
GL 7009S[e]	11.31 (2.26)	2.5 (0.7)	31.3 (7.8)[d]	4.9 (0.7)
Elias 16[e]	2.26 (0.16)	$\leq$1.4	$<$2.3	5.2 (0.5)
EC 118[e]	3.57 (0.35)	$\leq$1.4	$<$4.7	11.6 (1.4)

NOTE.—Uncertainties (1 σ) are indicated in parentheses and upper limits are of 3 σ significance.

[a] Detections and 3 σ upper limits of N(HCOOH) based on the 7.25 μm C$-$H deformation mode. Sources for which the 5.85 μm C=O stretching mode provides tighter constraints are indicated with "$\leq$."

[b] Assuming that both C3 and C4 components are due to NH_4^+, which is still a matter of debate (§ 6.1); integrated band strength $A = 4.4 \times 10^{-17}$ cm molecule^{-1} assumed (Schutte & Khanna 2003).

[c] The 13 μm H_2O libration mode used for $N(H_2O)$ determination (3 μm band in other cases).

[d] The 3.53 μm band provides a better or comparable constraint to $N(CH_3OH)$ than does the 9.7 μm band.

[e] Value obtained from or comparable to previous work or references therein: Dartois et al. (1999) (CH_3OH: W33A, GL 2136, W3 IRS 5, S140 IRS 1, NGC 7538 IRS 9, Mon R2 IRS 3, HH 100 IRS, GL 7009S), Boogert et al. (2000a) (CH_3OH: Elias 29), Boogert et al. (2004) (H_2O and CH_3OH: B5 IRS 1 and IRAS 08242$-$5050), Brooke et al. (1999) (H_2O: EC 90), Eiroa & Hodapp (1989) (H_2O: EC 82), Keane et al. (2001b) (H_2O: W33A, GL 2136, W3 IRS 5, S140 IRS 1, NGC 7538 IRS 9, Mon R2 IRS 3, HH 100 IRS, GL 989, GL 7009S), Knez et al. (2005) (H_2O and CH_3OH: Elias 16 and EC 118), Pontoppidan et al. (2004) (H_2O and CH_3OH: EC 92, SVS 4-5), Pontoppidan et al. (2005) (H_2O and CH_3OH: CRBR 2422.8$-$3423).

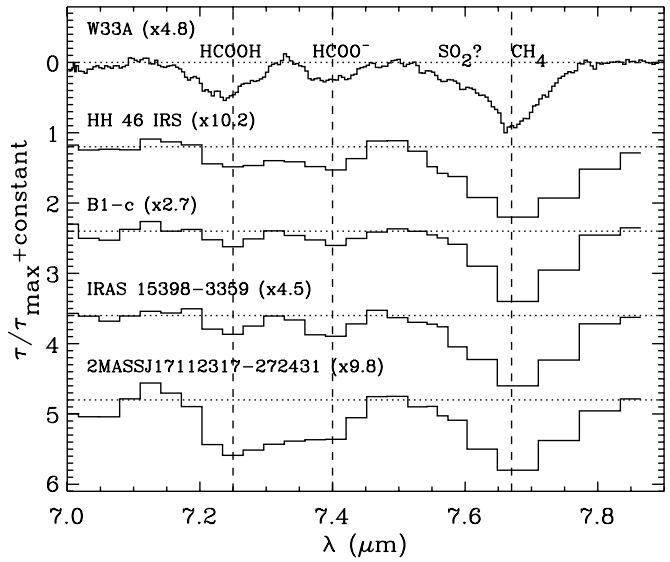

FIG. 11.—Optical depth 7–8 μm *Spitzer* IRS spectra of sources showing the 7.25, 7.40, and 7.67 μm features. The top source, W33A, is a massive YSO of which a higher resolution ($R = 800$) *ISO* SWS spectrum is shown. The features are labeled with their (possible) identifications.

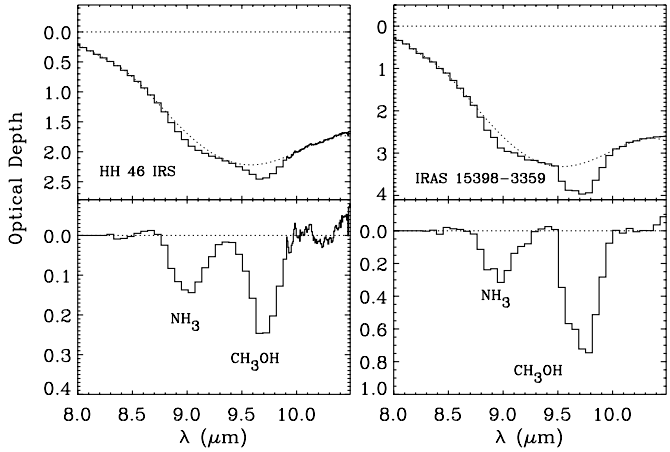

FIG. 12.—Features of solid NH_3 and CH_3OH in the spectra of the low-mass YSOs HH 46 IRS (*left*) and IRAS 15398−3359 (*right*). In the top panels for each source the dashed line indicates a local polynomial continuum, which was used to derive the optical depth plots in the bottom panels.

C3 ($\leq$30%). At the same time, Figure 15 also shows that component C5 and most of the prominent 6.85 μm absorption band (C3 and C4) are not accounted for. NH_4^+ is a candidate for the latter (§ 6.1), but its column density cannot be determined independently and thus this species is not included in this plot.

5.2. *Correlations*

To obtain further insight into the origin of the C1–C5 components, their strengths were normalized to the H_2O column density for the entire sample and plotted in Figure 16. As a measure of the degree of correlation, the ratios of the mean values and standard deviations were calculated (excluding upper limits), yielding values of 1.97, 1.70, 3.61, 1.35, and 0.87 for C1–C5, respectively. Thus, of all components, C3 correlates best with H_2O, followed by C1. The C2 and C4 components show more scatter, and, most interestingly, their strengths are largest at the lowest H_2O abundances. Component C5 correlates poorest with H_2O, especially when taking into account the tight 3 σ upper limits at the bottom end of the distribution. While, of all components, C5 is most susceptible to errors in the continuum determination, the C5/$N(H_2O)$ variation is too large to be explained by that alone (§ 4.2.2). Therefore, the large variations in the 6.0 μm excess (E_6; Fig. 7) can be ascribed primarily to variations in component C5, and much less to C1.

The different degrees of correlation of the C1–C5 components with H_2O indicate that they have different origins. To further elucidate their nature, their strengths were correlated with a number of tracers of the chemical or physical processing history of the ices. A well-known tracer is the ratio of broad and narrow 4.7 μm CO ice components (e.g., Chiar et al. 1998), often referred to as "polar" and "apolar" ices due to the mixing of CO with high and low dipole moment species, respectively. The apolar ices have a much lower sublimation temperature than the polar ices ($T_{sub} =$ 20 vs. 90 K), and thus their abundance ratio traces thermal processing. Higher temperatures are traced by the 15 μm CO_2 bending mode. Characteristic double peaks are visible in the crystalline ices produced after heating CO_2:H_2O mixtures to $T \geq 50$ K (Gerakines et al. 1999), and the fraction of crystalline CO_2 ice so derived for many sources in our sample is presented in Pontoppidan et al. (2008). Actual dust temperatures can be derived from far-infrared colors, but to trace the coldest dust components ($T < 20$ K), photometry at wavelengths >100 μm is required. For massive YSOs this was provided by *ISO* LWS spectra, and the far-infrared color was found to correlate with indicators of thermal processing (Boogert et al. 2000b). Unfortunately, such photometry is not available for most of our sample of low-mass YSOs. Tracers of ultraviolet radiation and cosmic-ray fluxes are even harder to obtain. Traditionally, the strength of the 4.62 μm absorption band has been used for this, since the carrier, an "XCN"-bearing species, was thought to be produced by the effects of UV photons or cosmic rays (e.g., Pendleton et al. 1999). Recent work shows, however, that the potential carrier OCN^- can be produced by heating an HNCO-containing ice formed at cold conditions by grain surface chemistry (van Broekhuizen et al. 2004). Thus, in this case the strength of the 4.62 μm band is in fact another tracer of thermal evolution.

The prominent 6.85 μm absorption band consists of independent short- and long-wavelength components (C3 and C4; Fig. 8), whose integrated optical depth ratio varies considerably (C4/C3 = 0.5–4). This essentially reflects abundance variations of the carrier of the C4 component because C4 correlates more poorly with the H_2O column density than does the C3 component (Fig. 16). The C4/C3 ratio is plotted against the observables discussed above, and while all of the observables show a large spread at C4/C3 $\leq$ 1.2, sources with stronger C4 components all have low solid H_2O and CO abundances (Figs. 17*a* and 17*b*). These include the low-mass YSOs IRAS 03301+3111 and DG Tau B and the massive YSOs Mon R2 IRS 3 and S140 IRS 1. The weakness of the ice bands in these particular sources hampers the correlation study with some of the above-mentioned observables: the ratio of the polar/apolar solid CO components and the fraction of crystalline CO_2 cannot be determined if these bands are not or weakly detected. Similarly, only a handful of OCN^- abundance determinations are available for these sources. It is thus concluded that the C4/C3 ratio is enhanced in environments that have low ice abundances. This is in agreement with earlier work on massive YSOs (Keane et al. 2001b), which showed an increase of the ratio in lines of sight with warmer dust temperatures. Potential carriers of the C4 and C3 components are discussed in § 6.1.

The strength of the enigmatic C5 component varies widely for both low- and high-mass YSOs. Toward massive YSOs, a trend

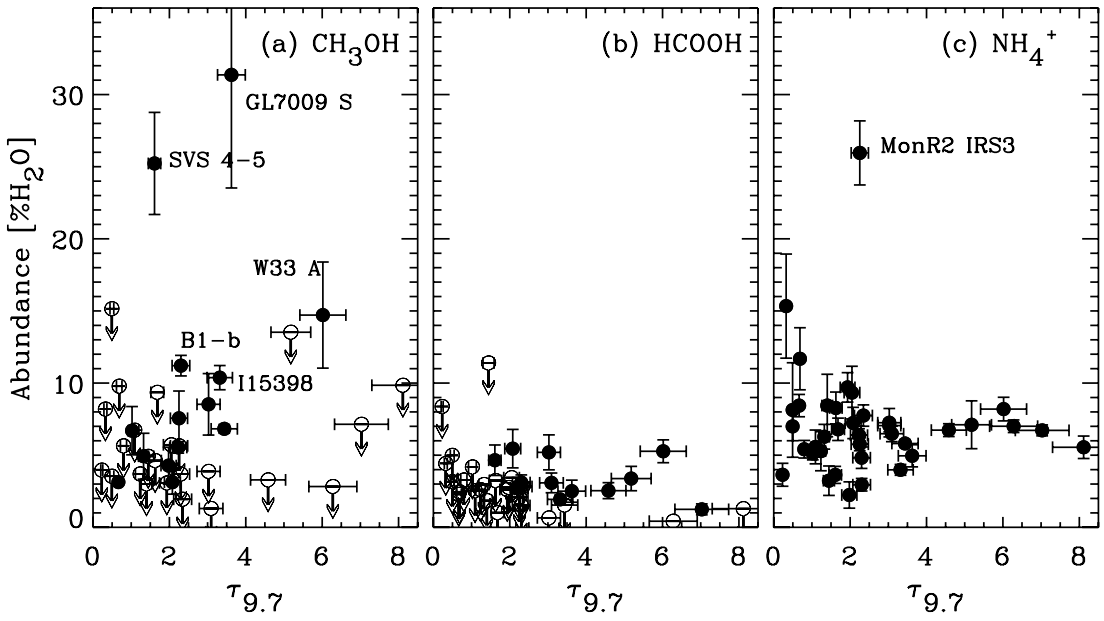

FIG. 13.—Abundances of (*a*) solid CH_3OH, (*b*) HCOOH, and (*c*) NH_4^+ in percentage of H_2O as a function of the 9.7 μm silicate band optical depth. The solid CH_3OH abundance is clearly more sight line dependent than the HCOOH abundance. Sources with the largest relative CH_3OH column densities are labeled in (*a*). Open symbols with arrows refer to 3 σ upper limits. Error bars are 1 σ. The NH_4^+ abundance in (*c*) was calculated assuming that both the C3 and C4 components are due to NH_4^+, but after subtracting the contributions from CH_3OH and H_2CO.

of increasing strength of the C5 component with the OCN^- abundance (4.62 μm feature) was claimed (Gibb & Whittet 2002), but in the current sample this trend is rather weak and is limited by the small number of sources with OCN^- detections (Fig. 18*e*). A stronger trend is observed with the ratio of the polar and apolar CO components: sources with strong C5 components show larger polar/apolar CO ratios (Fig. 18*c*). No correlations are observed with the H_2O, CO, and crystalline CO_2 abundances. Potential carriers are further discussed in § 6.2.

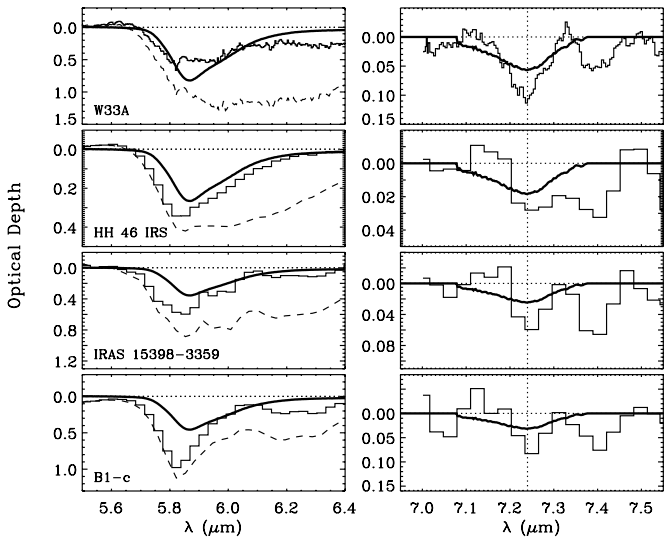

FIG. 14.—Comparison of laboratory solid HCOOH and interstellar spectra. The left panels show the region of the C=O stretching mode, the right panels the C−H deformation mode. From top to bottom four YSOs are shown with confirmed 7.25 μm absorption band detections (indicated with vertical dotted lines in the right panels). The histograms in the left panels represent component C1 of the interstellar spectra, i.e., after subtracting solid H_2O and components C2 and C5 defined in § 4.2.2. The dashed lines represent the spectra before C2 and C5 subtraction. In each panel the thick smooth line represents the laboratory ice mixture $HCOOH:H_2O:CH_3OH = 12:100:40$ at $T = 15$ K after removal of the H_2O bending mode (Bisschop et al. 2007). The laboratory spectra are scaled such that the integrated optical depth of the 7.25 μm band matches the observations. Note that the laboratory spectrum of the 7.25 μm band is wider than shown in Bisschop et al. (2007). This is due to a different baseline choice at the steep edge of the strong C−H deformation mode of CH_3OH in the laboratory data.

6. DISCUSSION

Long-standing key questions in astrochemistry concern the composition of the interstellar ices and the degree to which the composition of the ices is altered by heating and by the impact of

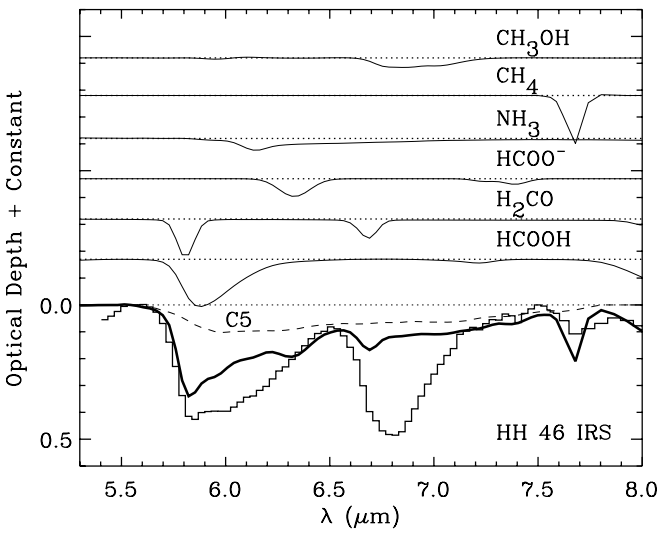

FIG. 15.—Simple species contributing to the 6 and 6.85 μm bands of the low-mass YSO HH 46 IRS, after H_2O subtraction [$N(H_2O) = 82.8 \times 10^{17}$ cm^{-2}]. Laboratory spectra of (*top to bottom*) solid CH_3OH, CH_4, NH_3, $HCOO^-$, H_2CO, and HCOOH were scaled to column densities derived independently elsewhere in the spectrum: 5.6% (CH_3OH), 2.2% (CH_4), 12.7% (NH_3), 0.4% ($HCOO^-$), 6.0% (H_2CO), and 2.0% (HCOOH) with respect to H_2O. These spectra were subsequently added to the underlying, unidentified C5 absorption component (*dashed line*), and the result is shown as a solid thick line. Clearly, the prominent 6.85 μm band is not explained by these particular species.

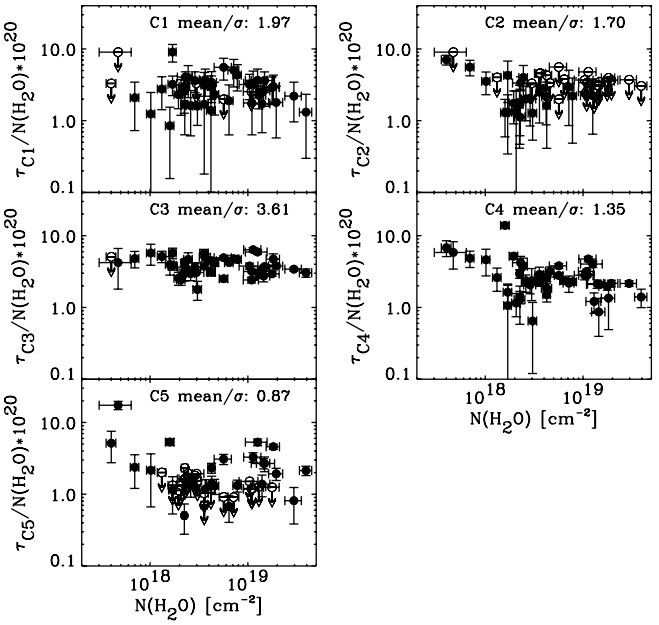

FIG. 16.—Peak optical depths of the 5–8 μm components (Fig. 8), normalized to $N(H_2O)$, plotted as a function of $N(H_2O)$. Error bars are 1 σ, but open symbols with arrows attached refer to 3 σ upper limits. At the top right of each panel the ratio of the mean over the standard deviation of the sample (excluding upper limits) is indicated. Component C3, i.e., the short-wavelength component of the 6.85 μm feature, correlates significantly better with $N(H_2O)$ than the other components do. Of the components that produce the 6.0 μm excess, C1 correlates better with H_2O than does C5. Note the increased strengths of C2 and C4 at low $N(H_2O)$.

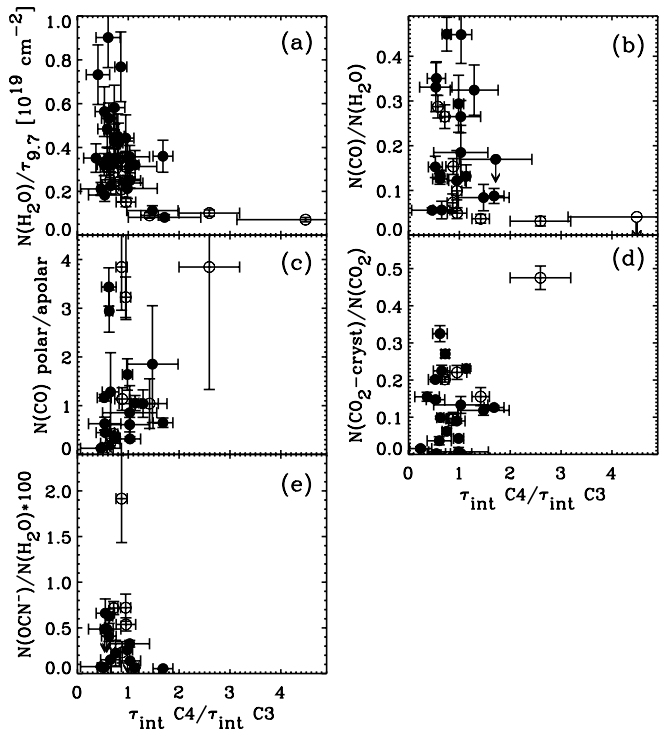

FIG. 17.—Ratio of the integrated strengths of components C4 and C3 (red and blue components of the 6.85 μm band) plotted against possible ice or dust temperature tracers. Along the y-axis are plotted (*a*) a measure of the solid H_2O abundance, (*b*) a measure of the solid CO abundance, (*c*) the polar/apolar solid CO ratio, (*d*) the fraction of crystalline CO_2 measured from the 15 μm bending mode, and (*e*) the relative abundance of the carrier of the 4.62 μm feature, OCN^-. Low-mass YSOs are indicated by filled circles, massive YSOs by open circles, and background stars by asterisks. Panels (*a*) and (*b*) show that sources with prominent C4 components have low ice (H_2O and CO) abundances.

energetic photons and cosmic rays. The 3–30 μm spectra presented in this paper extend studies addressing these questions from the previously well-analyzed massive YSOs to low-mass YSOs, as well as to background stars tracing quiescent cloud material. The 5–8 μm region exhibits a very rich absorption spectrum, which, apart from the O—H bending mode of H_2O, consists of at least five independent components. While most of component C1, much of C2, and part of component C3 are due to the simple species CH_3OH, HCOOH, NH_3, and H_2CO, the origin of a substantial amount of absorption is still unclear, and this is discussed in more detail below.

6.1. *Constraints on the Carrier(s) of Components C3 and C4 (the* 6.85 μm *Band)*

The 6.85 μm band was decomposed into "blue" and "red" components (C3 and C4). While C3 correlates tightly with the H_2O abundance, the relative strength of the C4 component increases at the lowest H_2O abundances (Fig. 16). This could be explained by the formation of a new species as the ices are heated and sublimate, or it could be a preexisting species that is less volatile than H_2O whose absorption band (C4) prevails at lower H_2O abundances. In the first scenario heating must play a role, and in the second it may. The detection of the C4 component in all YSOs and toward background stars favors the second scenario, in which the carrier is not formed by heating for its carrier exists already in the earliest stages of chemical evolution, i.e., in quiescent clouds. Higher dust temperatures in the vicinity of YSOs lead to sublimation and lower H_2O and CO abundances (Fig. 17), and the abundance of the carrier of the C3 component is reduced more rapidly than that of the C4 component.

Does the carrier of the C4 component survive in the diffuse interstellar medium (ISM)? A band at 6.85 μm is detected in lines of sight toward the Galactic center (GC), tracing a large column of diffuse dust (Chiar et al. 2000). However, its depth relative to the 9.7 μm silicate band ($\tau_{6.85}/\tau_{9.7} \sim 0.014$) is a factor of 5 less compared to the C4 component in the YSOs (factor of 10 compared to C3). The weak 6.85 μm band observed toward the GC sources is attributed to the C—H asymmetric deformation mode of aliphatic hydrocarbons (Chiar et al. 2000). Such aliphatic hydrocarbons have strong C—H stretching modes with distinct peaks at 3.38, 3.42, and 3.48 μm. A band at 3.47 μm is commonly detected toward YSOs (Brooke et al. 1999), but it does not show these distinct peaks and its depth relative to the 6.85 μm band is a factor of 3 weaker compared to the GC sources. Thus, although the carrier of the C4 component observed in our sample is (probably) less volatile than ices, it does not survive in the diffuse ISM. Conversely, the hydrocarbons observed in the diffuse ISM are not the carrier of the C4 component toward YSOs.

In a scenario proposed by Schutte & Khanna (2003) both the C3 and C4 components arise from an NH_4^+-containing ice. Its abundance would be typically 7% with respect to H_2O (Table 3 and Fig. 13), assuming the integrated band strength of 4.4×10^{-17} cm molecule^{-1} measured in Schutte & Khanna (2003). NH_4^+ ions can be produced either by acid-base reactions at low temperature (e.g., from NH_3:HNCO at 10 K; Raunier et al. 2004b) or by ultraviolet or cosmic-ray irradiation of simple mixtures (e.g., H_2O:CO_2:NH_3:O_2). The NH_4^+ band that is produced shifts to longer wavelengths on heating, i.e., from the peak wavelength of the C3 component to the peak wavelength of the C4 component. After additional energetic processing and H_2O sublimation, a salt is formed. Salts do not sublimate until temperatures of ~200 K

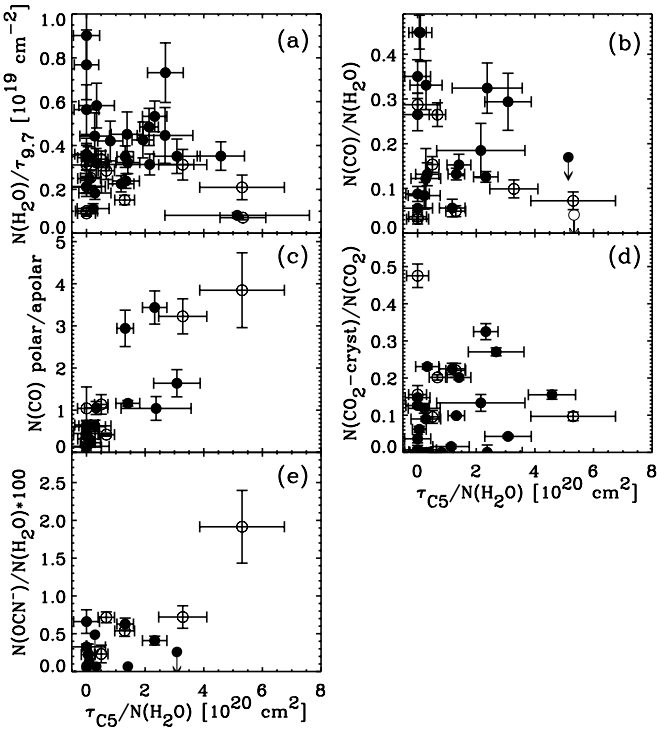

FIG. 18.—Peak strength of component C5 scaled to $N(H_2O)$ plotted against the same ice or dust temperature tracers as in Fig. 17. Possibly, enhanced polar CO (panel [*c*]) fractions are observed at larger C5 strengths.

(e.g., Schutte & Khanna 2003), significantly higher than the H_2O sublimation temperature of 90 K in space. The processed laboratory spectra show absorption at 6.0 μm due to anions (NO_2^-, NO_3^-, and HCO_3^-), some of which overlaps with the C2 components centered at ~6.15 μm that are observed in the YSOs with strong C4 components (Fig. 9; § 6.3). While these properties are consistent with the observations of YSOs, the presence of the C4 component toward all YSOs and background stars is hard to explain. In the experiments of Schutte & Khanna (2003) an NH_4^+ temperature of almost 200 K is required to match the peak position of this component. Such a high temperature can be excluded for many sources in the sample. Perhaps the impact of cosmic rays is responsible for the shift in peak position. Subsequent heating by nearby protostars leads to the observed increase in the C4/C3 ratio and eventually to the formation of a salt.

6.2. *Potential Carrier(s) of Component C5*

The enigmatic C5 component that stretches from 5.8 to ~8.0 μm is not due to NH_3, H_2CO, HCOOH, $HCOO^-$, or CH_3OH because these species do contribute to components C1–C4 (§ 5.1). Also, no correlation is found between the strengths of the C5 and the 6.85 μm red (C4) components. Therefore, these have unrelated origins. Heating might be involved in the formation of the carrier(s) of the C5 component (Fig. 18; § 5.2). Previously, three different origins were considered in the literature.

First, it should be noted that the shape of the average C5 component resembles that of the spectrum of solid H_2O (Fig. 10). It is particularly reminiscent of heated H_2O ($T > 120$ K) because of the weakness of the 6.0 μm peak with respect to the long-wavelength wing (e.g., Maldoni et al. 1998). While the shape of the 3 μm band indicates that heated ices are present along several lines of sight (e.g., RNO 91), its depth is, by the very definition of the C5 component, insufficient. Possibly, due to the effects of light scattering at the shorter wavelengths, a more direct path to the warm inner regions of the YSO is observed at 6 μm compared to 3 μm. Indeed, Monte Carlo radiative transfer models of a circumstellar disk show that at inclination angles of 70°–74° the depth of the 6.0 μm H_2O band is enhanced by a factor of 10 with respect to that at 3.0 μm (Pontoppidan et al. 2005). At higher inclinations, the enhancement is a factor of 3–4, while at lower inclinations the effect is negligible. Thus, the C5 component may be attributed to heated H_2O ice for some sources in our sample; for example, RNO 91 is known to possess an inclined disk (Weintraub et al. 1994) and has one of the most prominent C5 components. At the other extreme, the weakest C5 components are observed toward background stars (Table 2). Indeed, in these lines of sight the effect of scattering on the relative H_2O band depths is expected to be small due to the uniformity of the foreground clouds. For many YSOs with C5 absorption, however, independent observational evidence indicates that the scattering scenario is unlikely. For example, the CH_3OH column density derived from the 3.53 μm C—H stretching mode agrees well with that derived from the 9.7 μm C—H bending mode (§ 5.1.1; Schutte et al. 1991). Also, for high-mass YSOs the 4.25 and 15 μm bands provided solid CO_2 column densities that were in excellent agreement with each other (Gerakines et al. 1999), and in one line of sight also with the 2.7 μm CO_2 combination mode (Keane et al. 2001a). Thus, for these YSOs other explanations are required.

A second explanation of the C5 component could be the blend of negative ions suggested in Schutte & Khanna (2003). Ammonium (NH_4^+) and the anions HCO_3^-, NO_3^-, and NO_2^- are produced after UV photolysis or cosmic-ray bombardment of $H_2O/CO_2/NH_3/O_2$ ice mixtures. NH_4^+ has a strong band at 6.85 μm (i.e., components C3 and C4 in this work), but the bands of the anions overlap such that only one very broad feature is observed in the 5–8 μm range. While one may expect that in this scenario the C3/C4 and C5 components correlate well with each other, the observations show that they do not. Notably, the background stars have strong 6.85 μm components and little C5 absorption. The NH_4^+ ion can be produced after warming up a simple ice mixture too, however, while the HCO_3^-, NO_3^-, and NO_2^- anions may need more energetic input (Schutte & Khanna 2003). This may explain the large variation in the strength of the C5 component.

Third, extensive processing of simple ices by UV light or cosmic rays produces an organic refractory residue (Greenberg et al. 1995), whose blended O—H and C—H stretching and bending modes produce a feature similar to the C5 component (Gibb & Whittet 2002). Both this scenario and the blend of ions discussed above require a correlation of the strength of the C5 component with independent indicators of the presence of strong UV or cosmic-ray fluxes, which are currently unavailable. Also, both the organic residue and the salts are less volatile than the ices: they sublimate at temperatures ≤500 K in the laboratory (Schutte & Khanna 2003; Greenberg & d'Hendecourt 1985; $T_{sub} = 180$ K for H_2O ice). Therefore, one may expect C5 to be the main absorption component in the 5–8 μm region toward some YSOs where all H_2O ices have evaporated. Although in several sources the C5 component is the dominant contributor, it always is observed together with H_2O (except possibly toward L1448 IRS 1). Some H_2O may be trapped in the salt or organic residue at high temperatures, and some may be present in unprocessed foreground material. It is also important to note that, similar to C4 (§ 6.1), the C5 component is not observed in the diffuse ISM, confirming that their carrier(s) are not as refractory as silicates ($T_{sub} \sim 1500$ K).

Finally, it is noted that the C5 component may have a different origin in different lines of sight. An in-depth analysis of the physical conditions in specific lines of sight is required to discriminate

between the effects of disk orientation and the various ice processing mechanisms.

6.3. *Potential Carrier(s) of Component C2*

The C2 component spans the 6.0–6.4 μm wavelength range and is likely due to at least three different carriers. The N—H bending mode of NH_3 at 6.15 μm contributes 10%–50% to this band (§ 5.1.4). Another likely contributor is H_2O. Although the spectrum of pure, amorphous H_2O was subtracted from the 5–8 μm region before determining the various component strengths and profiles, the spectrum of interstellar H_2O may deviate from that of a pure, amorphous H_2O ice. The O—H bending mode of H_2O shifts to longer wavelengths and becomes significantly narrower, and its peak strength increases if the hydrogen bonding network in bulk amorphous H_2O ice is broken by the presence of other species (Ehrenfreund et al. 1996; Öberg et al. 2007). CO_2 is a realistic species because it is abundant (15%–40% with respect to H_2O) and a significant fraction is known to be mixed with H_2O (Pontoppidan et al. 2008; Gerakines et al. 1999). At sufficiently high CO_2 concentrations, the H_2O is located in small clusters, leading to monomer, dimer, and multimer bondings that produce a strong peak at 6.12 μm. The optical depth of the peak has been calculated for the YSO B5 IRS 1 (Öberg et al. 2007) and the background star Elias 16 (Knez et al. 2005) assuming that the H_2O ice along these lines of sight consists of two components: pure H_2O and the mixture $H_2O:CO_2 = 2:1$. It was found that when 25% of the H_2O is present in the latter, the 3 and 6 μm bands of H_2O and the 15 μm band of CO_2 are fitted simultaneously. Comparison with the C2 component in these sources shows that 20%–50% could be due to this effect. Thus, the short-wavelength side of the C2 component is both due to $H_2O:CO_2$ mixtures and due to NH_3. For the long-wavelength side, the C = O stretching mode of the $HCOO^-$ anion was previously considered, contributing $\leq$20% to the C2 strength (§ 5.1.5). Other anions, such as NO_2^-, NO_3^-, and HCO_3^- (§ 6.1), may contribute as well. These particular anions may be produced in the energetic processing of simple ices (Schutte & Khanna 2003), along with NH_4^+. Indeed, one of the most interesting observational aspects of the C2 component is that it becomes more pronounced for sources with stronger C4 components and lower H_2O abundances (Figs. 9 and 16). Overall the two components do not correlate very well, however, which is consistent with the result that three carriers of different nature contribute to the C2 component.

6.4. *Astrochemical Implications*

CH_3OH shows larger abundance variations with respect to H_2O than other solid-state species discussed in this work (HCOOH, H_2CO, NH_3). Tight 3 σ upper limits of a few percent are reported for a number of YSOs, but detections above the 10% level for others (Table 3 and Fig. 13). The solid HCOOH abundance is typically a factor of 2–3 lower than CH_3OH and does not show such large variations. If both CH_3OH and HCOOH are formed from CO by grain surface reactions, the lower HCOOH abundances are understood by the low atomic O/H ratio in the accreted gas and by the competition for O to react to CO_2 rather than with the formyl radical (HCO) to form HCOOH (Tielens & Hagen 1982). Indeed, large solid CO_2 abundances (15%–40% with respect to H_2O) are observed for a wide variety of YSOs (Pontoppidan et al. 2008). Grain surface chemistry does indeed appear a more likely formation mechanism than UV processing of the ices. First, while processing of simple ices by UV photons leads to CH_3OH formation, this process is not efficient enough to explain the enhanced abundances toward massive YSOs (Dartois et al. 1999), while for low-mass YSOs the UV flux is likely too low regardless. Second, HCOOH and CH_3OH are detected even in the most obscured sight lines in the sample. In fact, enhanced CH_3OH abundances are detected exclusively in some of the most embedded YSOs: the low-mass YSOs SVS 4-5, B1-b, and IRAS 15398–3359 and the massive YSOs W33A and GL 7009S (Dartois et al. 1999). SVS 4-5 is known to trace the envelope of the foreground Class 0 object SMM 4 (Pontoppidan et al. 2004). On the other hand, toward a few background stars tracing quiescent cloud material a low upper limit to the CH_3OH abundance was determined (Table 3; Chiar et al. 1996; Knez et al. 2005). Thus, it is suggested that, in the grain surface chemistry scenario, the CH_3OH abundance is enhanced at a time during the collapse (of some clouds) when the atomic O needed to form H_2O and CO_2 is exhausted, while still sufficient CO and H are available to form CH_3OH (Öberg et al. 2008).

While grain surface chemistry likely forms the simple neutral species, different mechanisms are required to produce the ions possibly responsible for several of the components in the 5–8 μm range. If the observed C3 and C4 components are indeed due to NH_4^+, its abundance is typically 7% with respect to H_2O (Fig. 13). The C4 component is observed even in the coldest sight lines. Indeed, low-temperature acid-base chemistry can efficiently produce NH_4^+ (Raunier et al. 2004b). The abundance of negative counterions needs to be addressed. While the C5 component could hide the necessary negative ions (Schutte & Khanna 2003), its strength does not correlate with the C3/C4 components. Further investigations on the presence of ions in the ices are crucial to understand the ice chemistry. Their physical properties are different from neutral species. Ions have higher sublimation temperatures, and thus the salts that are formed after the volatile species (e.g., H_2O and CO_2) have sublimated are able to survive at lower extinctions and then are subjected to harsher conditions, forming more complex species. For example, the biologically interesting species urea (H_2NCONH_2) is formed after the UV irradiation of an $NH_4^+OCN^-$ salt (Raunier et al. 2004a).

7. CONCLUSIONS AND FUTURE WORK

The present work extends the study of ices over the full 3–20 μm wavelength range from the previously well-studied massive YSOs ($\sim 10^5\ L_\odot$) to low-mass YSOs ($\sim 1\ L_\odot$). The following new insights were obtained:

1. Absorption features are detected at 6.0 and 6.85 μm in all sources, including high- and low-mass YSOs and background stars tracing quiescent cloud material. An empirical decomposition shows that the 5–7 μm absorption complex consists, in addition to the H_2O bending mode, of a combination of at least five independent absorption components.

2. In a subset of sources additional weak features are detected at 7.25, 7.40, 9.0, and 9.7 μm on top of the prominent Si—O stretching band of silicates. These features are associated with CH_3OH, HCOOH, NH_3, and possibly $HCOO^-$ and indicate abundances of 1%–30%, 1%–5%, 3%–8%, and 0.3% with respect to H_2O, respectively. The large source-to-source variations of the solid CH_3OH abundance are likely a result of the conditions at the time of grain surface chemistry.

3. Component C1 (5.7–6.0 μm) is mostly explained by solid HCOOH and H_2CO at abundances with respect to solid H_2O of typically 1%–5% and $\sim$6%, respectively.

4. Component C2 (6.0–6.4 μm) also likely arises from a blend of several species. Solid NH_3 can account for 10%–50% of the absorption. A similar amount can be attributed to absorption by monomers, dimers, and small multimers of H_2O mixed with a substantial amount of CO_2. The long-wavelength side of C2 is

potentially due to anions produced by acid-base chemistry (e.g., $HCOO^-$) or energetic processing. Indeed, a weak correlation with C4 suggests that the carriers of these bands (possibly salts) are related.

5. Components C3 and C4, the 6.85 μm band, show the same characteristics for low-mass YSOs and background stars as was previously found for massive YSOs by Keane et al. (2001b). Their ratio is empirically found to be dependent on dust temperature. The carrier of C4 is likely less volatile than that of C3 and than H_2O, but it is not observed in the diffuse ISM. These characteristics are also consistent with both components being due to NH_4^+ (ammonium ion). The detection of strong 6.85 μm bands toward deeply embedded YSOs and background stars requires a production at low temperature (acid-base chemistry or processing by cosmic rays), given the lack of heating sources and stellar UV fields.

6. The origin of the very broad component C5 (5–8 μm) is least understood. It is quite strong in several low- and high-mass YSOs, absent in others, and so far undetected toward background stars. It is possibly related to thermal processing, as a weak correlation with the ratio of the polar/apolar CO components is observed and its shape resembles that of warm H_2O. A blend of absorption by ions, as proposed by Schutte & Khanna (2003), which would require both heating and energetic processing of the ices, cannot be excluded. The latter could also lead to an organic residue, whose shape resembles that of the C5 component as well.

7. Weak correlations are found between the absorption components in the 5–8 μm range and tracers of physical conditions. A more thorough understanding of the conditions, the source geometry, and local radiation fields in specific lines of sight is required to further constrain the nature of the carriers (in particular for components C2–C5) and the importance of thermal and energetic processing. To what degree does scattering play a role? What are the dust temperatures, cosmic-ray fluxes, UV radiation fields, and timescales as a function of distance along the line of sight? Measurements of source fluxes above wavelengths of 100 μm with the *Herschel Space Observatory* will be valuable, as well as ground-based measurements of the 4.62 μm band of OCN^- in more lines of sight. In addition, further laboratory work, in particular on the effect of cosmic rays on the ices, especially for the identification of components C3 and C4, is required. Finally, study of the 5–8 μm features toward a larger sample of background stars is crucial to make further progress in the identification and processing history of interstellar ices.

We thank the anonymous referee for thoughtful comments on the manuscript and Alberto Noriega-Crespo for help in identifying the emission lines. Support for this work, part of the *Spitzer* Legacy Science Program, was provided by NASA through contracts 1224608, 1230779, 1230782, 1256316, and 1279952 issued by the Jet Propulsion Laboratory, California Institute of Technology, under NASA contract 1407. Astrochemistry in Leiden is supported by an NWO Spinoza grant, a NOVA grant, and by the European Research Training Network "The Origin of Planetary Systems" (PLANETS, contract HPRN-CT-2002-00308). The work of J. K. J. is supported by NASA Origins grant NAG5-13050. K. M. P. is supported by NASA through Hubble Fellowship grant 01201.01 awarded by the Space Telescope Science Institute, which is operated by the Association of Universities for Research in Astronomy, Inc., for NASA, under contract NAS 5-26555. We thank the Lorentz Center in Leiden for hosting several meetings that contributed to this paper. This publication makes use of data products from the Two Micron All Sky Survey, which is a joint project of the University of Massachusetts and the Infrared Processing and Analysis Center/California Institute of Technology, funded by the National Aeronautics and Space Administration and the National Science Foundation.

REFERENCES

Bernstein, M. P., Sandford, S. A., Allamandola, L. J., Chang, S., & Scharberg, M. A. 1995, ApJ, 454, 327
Bisschop, S. E., Fuchs, G. W., Boogert, A. C. A., van Dishoeck, E. F., & Linnartz, H. 2007, A&A, 470, 749
Bohren, C. F., & Huffman, D. R. 1983, Absorption and Scattering of Light by Small Particles (New York: Wiley)
Boogert, A. C. A., & Ehrenfreund, P. 2004, in ASP Conf. Ser. 309, Astrophysics of Dust, ed. A. N. Witt, G. C. Clayton, & B. T. Draine (San Francisco: ASP), 547
Boogert, A. C. A., Tielens, A. G. G. M., Ceccarelli, C., Boonman, A. M. S., van Dishoeck, E. F., Keane, J. V., Whittet, D. C. B., & de Graauw, T. 2000a, A&A, 360, 683
Boogert, A. C. A., et al. 1996, A&A, 315, L377
———. 2000b, A&A, 353, 349
———. 2004, ApJS, 154, 359
Brooke, T. Y., Sellgren, K., & Geballe, T. R. 1999, ApJ, 517, 883
Cazaux, S., Tielens, A. G. G. M., Ceccarelli, C., Castets, A., Wakelam, V., Caux, E., Parise, B., & Teyssier, D. 2003, ApJ, 593, L51
Chiar, J. E., Adamson, A. J., & Whittet, D. C. B. 1996, ApJ, 472, 665
Chiar, J. E., Gerakines, P. A., Whittet, D. C. B., Pendleton, Y. J., Tielens, A. G. G. M., Adamson, A. J., & Boogert, A. C. A. 1998, ApJ, 498, 716
Chiar, J. E., Tielens, A. G. G. M., Whittet, D. C. B., Schutte, W. A., Boogert, A. C. A., Lutz, D., van Dishoeck, E. F., & Bernstein, M. P. 2000, ApJ, 537, 749
Cox, P. 1989, A&A, 225, L1
Dartois, E., & d'Hendecourt, L. 2001, A&A, 365, 144
Dartois, E., Schutte, W., Geballe, T. R., Demyk, K., Ehrenfreund, P., & d'Hendecourt, L. 1999, A&A, 342, L32
Decin, L., Morris, P. W., Appleton, P. N., Charmandaris, V., Armus, L., & Houck, J. R. 2004, ApJS, 154, 408
Devlin, J. P., Sadlej, J., & Buch, V. 2001, J. Phys. Chem. A, 105, 974
d'Hendecourt, L., et al. 1996, A&A, 315, L365
Ehrenfreund, P., Gerakines, P. A., Schutte, W. A., van Hemert, M. C., & van Dishoeck, E. F. 1996, A&A, 312, 263
Eiroa, C., & Hodapp, K.-W. 1989, A&A, 210, 345
Evans, N. J., II, et al. 2003, PASP, 115, 965
———. 2007, Final Delivery of Data from the c2d Legacy Project: IRAC and MIPS (Pasadena: SSC)
Gerakines, P. A., Schutte, W. A., & Ehrenfreund, P. 1996, A&A, 312, 289
Gerakines, P. A., Schutte, W. A., Greenberg, J. M., & van Dishoeck, E. F. 1995, A&A, 296, 810
Gerakines, P. A., et al. 1999, ApJ, 522, 357
Gibb, E. L., & Whittet, D. C. B. 2002, ApJ, 566, L113
Gibb, E. L., Whittet, D. C. B., Boogert, A. C. A., & Tielens, A. G. G. M. 2004, ApJS, 151, 35
Gibb, E. L., et al. 2000, ApJ, 536, 347
Greenberg, J. M., & d'Hendecourt, L. B. 1985, in Ices in the Solar System, ed. J. Klinger et al. (Dordrecht: Reidel), 185
Greenberg, J. M., Li, A., Mendoza-Gomez, C. X., Schutte, W. A., Gerakines, P. A., & de Groot, M. 1995, ApJ, 455, L177
Greene, T. P., Wilking, B. A., André, P., Young, E. T., & Lada, C. J. 1994, ApJ, 434, 614
Grim, R. J. A., Baas, F., Greenberg, J. M., Geballe, T. R., & Schutte, W. 1991, A&A, 243, 473
Grim, R. J. A., & Greenberg, J. M. 1987, ApJ, 321, L91
Hagen, W., Tielens, A. G. G. M., & Greenberg, J. M. 1981, Chem. Phys., 56, 367
———. 1983, A&A, 117, 132
Houck, J. R., et al. 2004, ApJS, 154, 18
Hudgins, D. M., Sandford, S. A., Allamandola, L. J., & Tielens, A. G. G. M. 1993, ApJS, 86, 713
Keane, J. V., Boogert, A. C. A., Tielens, A. G. G. M., Ehrenfreund, P., & Schutte, W. A. 2001a, A&A, 375, L43
Keane, J. V., Tielens, A. G. G. M., Boogert, A. C. A., Schutte, W. A., & Whittet, D. C. B. 2001b, A&A, 376, 254

Kemper, F., Vriend, W. J., & Tielens, A. G. G. M. 2004, ApJ, 609, 826
Kerkhof, O., Schutte, W. A., & Ehrenfreund, P. 1999, A&A, 346, 990
Kessler-Silacci, J. E., Hillenbrand, L. A., Blake, G. A., & Meyer, M. R. 2005, ApJ, 622, 404
Knez, C., et al. 2005, ApJ, 635, L145
Lacy, J. H., Faraji, H., Sandford, S. A., & Allamandola, L. J. 1998, ApJ, 501, L105
Lahuis, F. 2007, Ph.D. thesis, Leiden Univ.
Maldoni, M. M., Smith, R. G., Robinson, G., & Rookyard, V. L. 1998, MNRAS, 298, 251
McLean, I. S., et al. 1998, Proc. SPIE, 3354, 566
Moore, M. H., & Hudson, R. L. 1998, Icarus, 135, 518
Moorwood, A. F. 1997, Proc. SPIE, 2871, 1146
Muñoz Caro, G. M., Meierhenrich, U., Schutte, W. A., Thiemann, W. H.-P., & Greenberg, J. M. 2004, A&A, 413, 209
Neufeld, D. A., et al. 2006, ApJ, 649, 816
Noriega-Crespo, A., et al. 2004, ApJS, 154, 352
Novozamsky, J. H., Schutte, W. A., & Keane, J. V. 2001, A&A, 379, 588
Öberg, K. I., Boogert, A. C. A., Pontoppidan, K. M., Blake, G. A., Evans, N. J., Lahuis, F., & van Dishoeck, E. F. 2008, ApJ, 678, 1032
Öberg, K. I., Fraser, H. J., Boogert, A. C. A., Bisschop, S. E., Fuchs, G. W., van Dishoeck, E. F., & Linnartz, H. 2007, A&A, 462, 1187
Palumbo, M. E., Pendleton, Y. J., & Strazzulla, G. 2000, ApJ, 542, 890
Pendleton, Y. J., Tielens, A. G. G. M., Tokunaga, A. T., & Bernstein, M. P. 1999, ApJ, 513, 294
Pontoppidan, K. M., Dartois, E., van Dishoeck, E. F., Thi, W.-F., & d'Hendecourt, L. 2003a, A&A, 404, L17
Pontoppidan, K. M., Dullemond, C. P., van Dishoeck, E. F., Blake, G. A., Boogert, A. C. A., Evans, N. J., II, Kessler-Silacci, J. E., & Lahuis, F. 2005, ApJ, 622, 463
Pontoppidan, K. M., van Dishoeck, E. F., & Dartois, E. 2004, A&A, 426, 925
Pontoppidan, K. M., et al. 2003b, A&A, 408, 981
———. 2008, ApJ, 678, 1005
Puetter, R. C., Russell, R. W., Willner, S. P., & Soifer, B. T. 1979, ApJ, 228, 118
Raunier, S., Chiavassa, T., Duvernay, F., Borget, F., Aycard, J. P., Dartois, E., & d'Hendecourt, L. 2004a, A&A, 416, 165
Raunier, S., Chiavassa, T., Marinelli, F., & Aycard, J.-P. 2004b, Chem. Phys., 302, 259
Schutte, W. A., Allamandola, L. J., & Sandford, S. A. 1993, Icarus, 104, 118
Schutte, W. A., & Khanna, R. K. 2003, A&A, 398, 1049
Schutte, W. A., Tielens, A. G. G., & Sandford, S. A. 1991, ApJ, 382, 523
Schutte, W. A., et al. 1996, A&A, 315, L333
———. 1999, A&A, 343, 966
Skinner, C. J., Tielens, A. G. G. M., Barlow, M. J., & Justtanont, K. 1992, ApJ, 399, L79
Skrutskie, M. F., et al. 2006, AJ, 131, 1163
Tielens, A. G. G. M., Allamandola, L. J., Bregman, J., Goebel, J., Witteborn, F. C., & d'Hendecourt, L. B. 1984, ApJ, 287, 697
Tielens, A. G. G. M., & Hagen, W. 1982, A&A, 114, 245
van Broekhuizen, F. A., Keane, J. V., & Schutte, W. A. 2004, A&A, 415, 425
Watson, D. M., et al. 2004, ApJS, 154, 391
Weintraub, D. A., Tegler, S. C., Kastner, J. H., & Rettig, T. 1994, ApJ, 423, 674
Werner, M. W., et al. 2004, ApJS, 154, 1
Whitney, B. A., Wood, K., Bjorkman, J. E., & Wolff, M. J. 2003, ApJ, 591, 1049
Whittet, D. C. B., Shenoy, S. S., Bergin, E. A., Chiar, J. E., Gerakines, P. A., Gibb, E. L., Melnick, G. J., & Neufeld, D. A. 2007, ApJ, 655, 332
Whittet, D. C. B., et al. 1996, A&A, 315, L357
Wilking, B. A., Bontemps, S., Schuler, R. E., Greene, T. P., & André, P. 2001, ApJ, 551, 357